Climate-driven deposition of water ice and the formation of mounds in craters in Mars' North Polar Region

Susan J. Conway, Niels Hovius, Talfan Barnie, Jonathan Besserer, Stéphane Le Mouélic, Roberto Orosei, Natalie Anne Read

Climate-driven deposition of water ice and the formation of mounds in craters in Mars' North Polar Region

Susan J. Conway*
Laboratoire de Planétologie et Géodynamique de Nantes UMR-CNRS 6112,
Université de Nantes, 2 rue de la Houssinière, BP92208, 44322 Nantes, France.
susan.conway@univ-nantes.fr

Niels Hovius
Dept. of Earth Science, University of Cambridge UK, CB2 3EQ.
nhovius@esc.cam.ac.uk

Talfan Barnie
Dept.of Geography, University of Cambridge UK, CB2 3EN.

Jonathan Besserer
Laboratoire de Planétologie et Géodynamique de Nantes UMR-CNRS 6112,
Université de Nantes, 2 rue de la Houssinière, BP92208, 44322 Nantes, France.

Stéphane Le Mouélic
Laboratoire de Planétologie et Géodynamique de Nantes UMR-CNRS 6112,
Université de Nantes, 2 rue de la Houssinière, BP92208, 44322 Nantes, France.

Roberto Orosei

Istituto di Astrofisica Spaziale e Fisica Cosmica (IASF), Italy

Natalie Anne Read

Dept. of Earth Science, University of Cambridge UK, CB2 3EQ.

*Corresponding author

Short title: A climatic origin of crater-ice in Mars' North Polar Region

Abstract

This paper explores the origins and evolution of ice-rich interior mounds found within craters of the north polar region of Mars. We present a systematic study of impact craters above 65°N, and identify 18 craters that have interior mounds. At least eleven of these mounds are composed of water ice and geometric similarities suggest that dune-covered mounds may also have a water ice core. The mounds are found in the deeper craters in the north polar area and we suggest that these form a specific microclimate favorable for mound initiation and growth. It is likely that at least seven of the mounds have evolved as individual outliers, rather than conterminous with the main polar cap. Our observations suggest that the mounds are built up by atmospheric deposition, similar to that of the north polar layered deposits. Using a combination of remote sensing techniques enabling topographic, spectral, radar and image data analyses, we have documented the morphology, composition and stratigraphy of selected mounds. We advance and test four hypotheses for formation of these mounds: artesian outpouring from a deep aquifer, hydrothermal activation of ground ice, remnants of a more extensive polar cap, and atmospheric deposition on ice caps in meteorologically isolated locations. We propose that during periods when the perihelion was located in northern summer (most recently 10-25 ka before present) the microclimate in these craters retarded the sublimation of CO_2 and water ice in northern spring, thus creating a cold trap for volatiles released as the seasonal cap retreated. This created a thick enough deposit of water ice to withstand sublimation over the summer and initiate a positive feedback leading to mound-building. Mounds without complete dune-cover may be in dynamic equilibrium with the ambient climate and show evidence of both present-day and past periods of erosion and aggradation. We conclude that the water ice mounds formed in deep impact craters in Mars' north polar region may contain sensitive records of past polar climate that may enhance our understanding of the CO_2-H_2O system in the polar regions.

Keywords: Mars; ices; Mars, polar geology; Mars, climate; Cratering.

Highlights:

- 18 potentially ice-cored mounds were found in craters in Mars' north polar region.
- The stratigraphy of the mounds argues for deposition from the atmosphere.
- We argue many of them were deposited separately from the polar cap.
- The crater micro-environment is a potential explanation for mound initiation.
- These mounds are sensitive and important records of Amazonian climate on Mars.

1. Introduction

The northern lowlands of Mars have long been considered an important reservoir for water. It has been suggested that a northern ocean existed there in the Noachian and that water may now be present deep in the local subsurface (e.g., Clifford, 1993; Clifford and Parker, 2001; Perron et al., 2007). More pertinently, the northern polar cap, with an estimated volume of 1.3 x 10^6 km^3 (Selvans et al., 2010) consists of a mixture of water ice and dust, and a region of near-surface ground ice extends down to latitudes of 45° (Byrne et al. 2009). This was first shown by the hydrogen ion signature found by gamma ray spectrometry (Feldman et al., 2004; Jakosky et al., 2005) and later supported by spectral signatures from OMEGA (Bibring et al., 2005), the distribution of water surface frosts (Vincendon et al., 2010), the distribution of fluidized craters (Barlow and Perez, 2003) and the radar reflectivity properties of the surface (Mouginot et al., 2010), with ice found by the Phoenix lander (Mellon et al., 2008) providing a local ground truth. Seasonal cycles mobilize and redistribute these surface volatiles; principally those exposed on the polar cap. At present, the most noticeable seasonal change is the waxing and waning of the so called 'seasonal' polar caps, observable from Earth (e.g., Antoniadi, 1930). The northern hemisphere seasonal cap commonly extends down to 50°N and consists primarily of CO_2 ice. It has a thickness of ~ 0.5 m (Cull et al., 2010; Smith et al., 2001), and is sourced from the atmosphere by condensation of water followed by CO_2 (Ivanov and Muhleman, 2001). Deposition occurs during the polar night and so has not been directly observed, but is thought to involve atmospheric condensation possibly as snow from ubiquitous cloud-cover. The spring recession is better characterized and it comprises a gradual northward retreat first of the CO_2, then of the thinner water-ice annulus (Bibring et al., 2005; Wagstaff et al., 2008).

After recession of the seasonal volatile deposits there remain several substantial outliers composed of water ice, which are spatially separated from the northern polar cap (Langevin et al., 2005; Tanaka et al., 2008). Many of these ice bodies are found within craters, e.g.,

93 Korolev, Dokka and Louth. They are morphologically distinctive (Garvin et al., 2000), forming
94 an interior mound, which is convex-up and dome-shaped, with low local slopes and a moat
95 that separates it from the crater walls. These mounds are distinct from an impact central
96 peak, because they have convex-up positive relief in the center, often with a large volume
97 placed asymmetrically within the crater. These mounds are generally assumed to be
98 remnants of a previously more extensive northern ice cap (Garvin et al., 2000; Tanaka et al.,
99 2008). Other possible origins include: upwelling from an underground aquifer (proposed but
100 not supported by Russell and Head, 2002), activation of near-surface ground ice by impact-
101 induced hydrothermal systems (a possibility considered for paleolake formation by Osinski et
102 al., 2005; Rathbun and Squyres, 2002) and atmospheric condensation as individual outliers
103 of the main cap (Brown et al., 2008). Although the latter invokes atmospheric deposition, as
104 for the polar cap, it differs significantly from the formation of polar cap remnants in that 1) a
105 larger extent of the polar cap is not required and 2) more importance is given to
106 microclimatic effects inside the craters. Each of these formative mechanisms has important,
107 but different, implications for the dynamics of Mars' hydrosphere and climate. For example, if
108 they are indeed remnants of a formerly more extensive polar cap, then these mounds are
109 important records of both its extent and the conditions needed to preserve this ice. If sourced
110 from near-surface, or deep ground-ice, then the mounds give information on the distribution
111 of this ice and an indication of the volumes of water stored in the Martian crust. If the
112 mounds are supplied from deep sources, then this could support the presence of a deep,
113 global hydrosphere (Clifford, 1993). And if they are individual cap outliers, then the mounds
114 could be sensitive to climate perturbations and hence, their spatial distribution, morphology
115 and internal structure can help place constraints on recent climate.

116 The aim of this study is to explore the origins and evolution of interior mounds that are found
117 within some craters in the North Polar region of Mars. To this end, we document and
118 interpret the distribution, morphology and internal structure of these mounds, finding that the

majority have likely formed by atmospheric deposition triggered by microclimatic effects inside the host craters, separate from the main polar cap.

2. Approach

2.1 Craters in the north polar basin

We have based our impact crater survey on information from the Mars Orbiter Laser Altimeter (MOLA) gridded data at 256 and 128 pixels per degree for the north polar region, recording the locations and morphometric properties of all craters that are hydrologically intact including craters with internal mounds. This survey is complete for craters with a diameter >5 km, located north of 65°N (Barnie, 2006).

Impact craters were identified and digitized from MOLA data using a watershed analysis technique aimed at delineating crater rims (*cf.* Stepinski et al., 2009). Each crater was given a unique identifying number (Barnie, 2006; Hovius et al. 2009). Based on visual inspection of the Thermal Emission Imaging System (THEMIS) and Mars Orbiter Camera Narrow-Angle (MOC-NA) image mosaic data we identified craters containing dune fields. Dune fields were identified by morphology where image resolution was sufficient and elsewhere by a characteristic combination of high IR emission values in THEMIS IR daytime data and low reflection of visible light in THEMIS VIS.

For all impact craters in our catalogue, we obtained elevation statistics from the MOLA digital elevation model (DEM) including the maximum, minimum and range. The latter was used as an estimate of the overall crater depth. The mean crater diameter was calculated by using $D = 2\sqrt{(A/\pi)}$, where D is the diameter and A the area of the digitized rim polygon. This method assumes the rim traces a circle and is not biased by topographic irregularities or slight obliquity of the crater-form. The distance from a crater to the polar cap was measured along the shortest straight line from the crater centroid to the edge of the contiguous Polar Layered Deposits and Polar Ice Deposits as mapped by Tanaka et al. (2005).

From our catalogue, we have isolated all craters containing raised central topography for further analysis. The following additional criteria were applied:

1. To identify and exclude central peaks: North-south and east-west topographic profiles were taken across these craters. Craters with central peaks were recognized by the small extent (< 10% of the crater floor) and central position of the rise and the similarity of rise and crater wall albedo. These craters were not considered further.
2. For the remaining craters where the presence of dark dunes dominated the albedo of deposits within a crater, we applied a minimum relief of 150 m in our identification of mounds. This is the maximum relief of inner-crater dunefields measured outside of the survey area, and the cut-off eliminated only one mound from our survey (marked 332 in Fig. 2).

As the resulting mounds have geometries and surface attributes distinct from those of central peaks, they were deemed to be depositional in origin. We digitized the limit of the mounds using the topographic inflexion at the transition to concave-up crater topography as a guide. Mound volume was estimated from surface topography and an extrapolation of the crater floor below the mound (not including any estimate of a central peak). This involved rotating through 360° the power-law best fit to the median radial profile of the crater interior (excluding any areas containing the mound) and differencing this estimated surface with the MOLA topography to generate an isopach map for each mound. Using this map we also calculated the mound asymmetry by measuring the horizontal offset between the center of mass of the mound and the centroid of the crater rim.

2.2 Mound Composition

We have investigated the composition of surface materials on the crater mounds using data from Mars Express' Observatoire pour la Minéralogie, l'Eau, les Glaces et l'Activité (MEX OMEGA) imaging spectrometer and Mars Reconnaissance Orbiter's Compact

169 Reconnaissance Imaging Spectrometer for Mars (MRO CRISM) targeted observations to
170 compute simple diagnostic ratios, including band depth and drop-off. OMEGA has a nearly
171 complete coverage of the north polar region at a spatial resolution of ~3 – 7 km/pix and also
172 covers selected areas at 0.5 - 1.5 km/pix. CRISM targeted observations have much lower
173 global coverage, but a very high spatial resolution of 15.7 - 19.7 m/pix. Both datasets
174 underwent standard atmospheric correction before spectral analysis ("volcano-scan"
175 algorithm, cf. Morgan et al., 2009). Although aerosol effects, not accounted for in this
176 correction, can be important in the north polar region (Vincendon et al. 2006; Vincendon
177 2008), the strong reflectivity of water and CO_2 ice overwhelms the atmospheric effects
178 allowing reliable identification (Brown et al., 2010). Datasets from northern summer (Solar
179 longitude, L_s 90 - 120°) were used to avoid seasonal CO_2 surface frost, which could mask
180 any spectral signals from the material beneath (Bibring et al., 2005). The relative depth of
181 the absorption band at 1.50 µm was used to estimate the water ice content. The depth of the
182 absorption band at 2.35 µm was used to estimate the quantity of carbon dioxide ice (Brown
183 et al., 2010).

184 2.3 Internal Stratigraphy

185 The stratigraphy of mound materials was investigated with image data of surface outcrops
186 and radar data capturing the interior stratigraphy. Surface stratigraphic information was
187 obtained from images collected with THEMIS, High Resolution Stereo Camera (HRSC on
188 Mars Express), MRO Context (CTX) and MRO High Resolution Imaging Science Experiment
189 (HiRISE). All these images were either already geometrically corrected (HiRISE, HRSC), or
190 corrected using routines in the software ISIS3. Alignment with the MOLA DEM was manually
191 checked by verifying that local highs and local lows (e.g., crater rims, troughs) corresponded
192 between the image and the MOLA data. For specific examples we measured the distance
193 between the layers in plan-view. We assumed that the layers were approximately flat-lying
194 and thus corrected the measured distances to account for exposure angle (which makes the

195 plan-view width of layers wider than their true thickness if the slope is less than 45°). This
196 was done by measuring the local slope, derived from MOLA topography, in the same
197 orientation as the layer thickness measurements. As the length scale of the MOLA-derived
198 slope is approximately ten times larger than that of the measured layers, the slope correction
199 introduces a degree of error, however it affects all measurements and no better source of
200 topography is available at present. For comparison purposes, we made equivalent
201 measurements of layer thickness in three exposures of the Polar Layered Deposits (PLD) in
202 HiRISE images PSP_010366_2590, TRA_000825_2665 and TRA_000863_2640 and one
203 exposure of the Basal Unit (BU) in HiRISE image TRA_000863_2640.
204 At selected locations we measured the junction angles of angular unconformities and/or
205 discontinuities exposed in outcrop, and ascertained younging directions from the layer
206 geometry. Where possible, dip and strike measurements of large-scale layering were made
207 by employing the geometric relationships between individual layers and 25 or 50 m contours
208 derived from the MOLA 512 and 256 pixels per degree data (~115 and ~230 m/pix,
209 respectively). Dips and strikes were measured over a length-scale of kilometers, so should
210 be considered as an area average value. We estimate the error in the dip measurement to
211 be 1-2° as detailed below.
212 Uncertainty in the dip measurement derives from: 1) errors in the layer digitization, 2) human
213 errors in the distance measurements and 3) errors in the contours. We consider the layers to
214 be digitized to within 2 pixels of their actual location on the images (50 cm for HiRISE and
215 12 m for CTX). We estimate the horizontal uncertainty of our distance measurements due to
216 human error as being between 10 and 50 m, thus greater than the digitization uncertainty.
217 Horizontal errors of this magnitude (over lengthscales of kilometers) account for at worst a
218 2° error in dip, but usually ±1°. Contour errors can originate from interpolated pixels in the
219 MOLA DEM and misalignment of the DEM with the images. The interpolated pixels are a
220 relatively small source of error, because we performed these measurements over smooth,
221 continuous surfaces for which interpolation performs well, resulting in smooth contours with

regular intervals. The potential horizontal misalignment between the images and DEM dominates the error and we estimate it is of the order of 1-2 MOLA pixels (460 m at worst, but more likely 100-200 m). However this does not necessarily change the horizontal distance between the contours (and thus the dip measurement) unless the slope changes significantly over distances of 460 m or less in the region of measurement. For the majority of measurements this was not the case. However, we took three examples where this was the case (one in Korolev and two in crater 663) and shifted the contours in relation to the images by ±460m in the direction of greatest change in slope. This simulated "worse-case" misalignment resulted in an error in the measured dip angle of ±1.5°.

We inspected all available MRO Shallow Radar (SHARAD) data intersecting craters with mounds for signs of internal structure. Where we found structure within mounds we performed clutter simulations using MOLA data to confirm that observed structures were not due to surface topographic effects (Russo et al., 2008). To assess layer spacing and thickness of mound deposits we converted the two-way-time into depth (cf. Plaut et al., 2009) using a permittivity of 3.15 as previously used by Putzig et al. (2009) for the nearly pure ice of the polar cap.

3. Results

3.1 Northern plains craters morphology and distribution

We found 397 craters with a diameter > 5 km north of 65°N. The depth-diameter relationship for these craters is shown in Fig. 1. The relationship is described by $d = 0.05D^{0.98}$, where d is crater depth (km) and D is crater diameter (km). For comparison, Garvin et al. (2000) found $d = 0.03D^{1.04}$ for 109 impact craters north of 57°N. These relationships differ significantly from the global depth-diameter relationship for pristine craters as determined by Garvin (2005). Compared to the polar depth-diameter relationships, the global depth-diameter relationship predicts deeper craters for a given diameter, apart from for the very largest

247 diameter craters. The same trend has been noted by Boyce and Mouginis-Mark (2005) and
248 Kreslavsky and Head (2006). This suggests that in the north polar area either, craters have
249 been subject to significant infilling, or that the properties of local substrate differ substantially
250 from the rest of Mars such that on formation impact craters are shallower compared to the
251 global population. From morphological evidence and the existence of a small population of
252 deep, young craters both Boyce and Mouginis-Mark (2005) and Kreslavsky and Head (2006)
253 conclude that craters in the north polar area are infilled.

254 At least 38 craters with D > 5 km contain dune fields. Dune fields were found in 28% of
255 craters > 400 m deep (Fig. 1), but not in shallower craters. Such dune fields are not
256 restricted to the polar region; we have found them in 24% of craters between 50°N and
257 65°N. At these latitudes, the relief of dune fields above the crater floor usually does not
258 exceed 150 m and the deposits usually cover relatively small areas within a crater. At higher
259 northern latitudes some craters have extensive dune cover. This includes some craters with
260 depositional mounds with relief in excess of150 m.

261 According to our criteria, eighteen craters were found to contain mounds (Fig. 2). They are
262 located between 70°N and 82°N, and none are smaller than 9.5 km in diameter (Table 1).
263 Seven are adjacent to the polar cap and the furthest is located > 600 km from the cap. No
264 craters with mounds were found between 65 and 70°N. Many of the mounds consistently
265 have high albedo in summer months (e.g., Armstrong et al., 2007; Garvin et al., 2000).
266 However, many other craters in the north polar region that do not contain interior mounds
267 also have this attribute (Calvin et al., 2009; Seelos et al., 2008; and informally by the MRO
268 HiRISE team). Craters with mounds lie within the general depth-diameter distribution of
269 craters in this region (Fig. 1), but for a given diameter they are relatively shallow compared
270 to other craters of the same diameter. This can be accounted for only in part by the presence
271 of a mound (predicted depths are given in Table 1 and shown on Figs. 1 and 3). Moreover,
272 mounds are not found in all craters of any particular diameter and not all craters at a given

latitude with a similar diameter contain a mound. In fact only 24% of all craters located above 70.1°N with diameters greater than 9.5 km have interior mounds.

Figure 3 shows two representative examples of impact craters with an interior mound (all the craters are shown in Fig. S1). Firstly, Dokka (388) with a clean ice mound, like Korolev (206) and six other, smaller craters in our survey and secondly crater 811 with a mound-shape similar to Dokka's, but entirely covered by dunes ("complete dune cover" on Fig. 2). Crater 814 shares this characteristic. Four other craters have complete dune coverage, but their mounds do not span the whole crater floor (480, 882, 904 and 934 – "dune covered mounds" on Fig. 2). There are four mounds with dune partial cover, including one in crater 503, Louth. In all cases dune patches coincide with the topographic high and only in the cases where there is complete dune cover do the dunes ingress into the moat. Despite the different levels of dune cover the mounds share the following morphological characteristics (Fig. S1): flat or gently sloping summit, asymmetrical placement and a partial or complete moat separating the mound from part or all of the crater wall.

At the scale of MOLA resolution (~230 m) the mounds are smooth (except where dunes are present, Fig. 3) and gently domed, with maximum local slopes of up to 34° and a half-range modal slope for all the mounds of 0.9° (mean of 3.6°). Mound relief ranges from 103 m to 1818 m above the current crater floor and mounds extend to within 13 – 1388 m below the crater rim, filling their host to 9 – 89 % of current crater depth from rim to floor (Table 1). Pole-centered, radial swath profiles including the craters containing mounds illustrate the local penetration depths of these craters into the crust and the relative heights of the mound summits (Fig. 4). The longitudinal extent of the swaths was chosen to minimize the longitudinal variation in elevation, so the penetration depth of the craters can be clearly seen. Figure 4 shows that the craters with mounds tend to be within the craters that penetrate to the deepest level for a given latitude and longitude region, but also that not all

298 of the deeply penetrating craters have mounds. This figure also demonstrates that there is
299 no characteristic height up to which the mounds extend vertically.

300 Estimates of maximum ice thickness range from 94 to 1890 m with a mean of 605 m, and
301 mound volumes range from 0.8 to 3850 km^3, with a mean of 315 km^3 (Table 1 and Fig. 5).
302 Our volume estimates are higher than those calculated by Garvin et al. (2000) for the largest
303 craters. For example Garvin et al. (2000) listed volumes of 1356 and 463 km^3 for the infill of
304 Korolev and Dokka, respectively and our corresponding estimates are 3850 and 1320 km^3
305 (Table 1). The discrepancy can be accounted for by the difference of methods used in this
306 study and that of Garvin et al. (2000). Garvin et al. (2000) used single MOLA profiles to
307 determine a polynomial fit to the cavity interior and constrained the predicted depths using
308 empirical relationships between depth and diameter derived from 109 craters in the region.
309 We used all available MOLA data to provide information on the cavity shape and did not
310 constrain the crater depth.

311 Mounds are either completely or partially surrounded by a moat. Similar moats have been
312 found around concentric crater fill (CFF) near the Martian dichotomy boundary (Levy et al.,
313 2010). However, CFF is flat-topped, rough at MOLA resolution (~ 20-80 m of relief) and has
314 not been found to extend above ~450 m below the crater rim. Westbrook (2009) described
315 75 craters in the south polar region, which also contain mounds. These mounds are similar
316 to those described here in that they have a flat top, a distinct bounding slope (a moat), are
317 often offset from the crater center, 35 of them have exposed ice and layers and 17 are
318 topped by sand dunes. Notable differences include: the south polar mounds often have a
319 bounding ridge encircling their flat top, some exhibit flow features, some have multiple
320 superposed mounds, they are found down to lower latitudes (60.8°S) and their host craters
321 are larger (diameters range from 18.6 to 114.1 km, mean 45.1 km). With the exception of the
322 southern polar craters, mounds such as the ones described here have not been reported
323 elsewhere on Mars.

3.2 Mound composition results

Spectral data acquired by OMEGA (Fig. 6) show that there are very high water-ice concentrations (up to ~0.7 band depth) at the surface of the mounds in Korolev (206), Dokka (388), Louth (503) and unnamed craters 544 and 579. The CO_2 ice signal of from the 2.35 μm band depth is less than 0.2, hence at the limits of the detection using this method. This indicates that the mounds are predominantly composed of water ice, similar to the inferred composition of the north polar cap (Bibring et al., 2005). The other mounds in our survey are too small to be resolved in low resolution OMEGA tracks and are not covered by high resolution tracks. Where possible we have used CRISM targeted images to investigate the composition of the mounds. For seven of the craters CRISM targeted images were not available in the summer season, or of insufficient quality (obscured by clouds or other atmospheric phenomena). Mounds that are completely covered in dunes had no discernible water ice signal during northern summer. Instead their spectra resembled those of background dust. For two mounds with partial dune cover (craters 663 and 769), a weak water ice signal was detected in high albedo patches, but this signal was not significantly stronger than that of the surrounding plains or crater interior. For crater 769 in particular the spectra across both available images (FRT0000b546 and FRT0000cf48) were dominated by dust, possibly due to the occurrence of small dust storms before these spectra were taken. These storms were observed in Mars Color Imager (MARCI) images (Malin, et al., 2008. MRO MARCI Weather Report for the week of 30 June 2008 – 6 July 2008. MSSS-40, http://www.msss.com/msss_images/2008/07/09/ and MRO MARCI Weather Report for the week of 13 October 2008 – 19 October 2008. MSSS-55, http://www.msss.com/msss_images/2008/10/22/). However, by inspecting the map of surface water ice abundance of Brown and Calvin (2010) derived from analysis of CRISM mapping data, we were able to confirm the presence of water ice in craters:332, 515, 577, 663, 697 and 795, whereas 436, 480 and 769 had no water ice signal.

Spectral instruments (such as OMEGA and CRISM) can only penetrate the optical surface and give information on the composition of the top few microns of the substrate in the case of rock or dust, and the top few centimeters in the case of ice (Brown et al., 2010). Hence the signals that we have observed could be from a thin surface veneer. However, other lines of evidence support the hypothesis that the mounds are composed of a substantial thickness of water ice, notably radar and stratigraphic arguments presented in Section 3.3 and also thermal arguments in Section 4.5.1. Having confirmed the presence of water ice in eleven of the crater mounds and having found striking morphometric similarities in all 18 mounds, including craters completely covered by dunes, we propose that all these mounds have a similar composition.

3.3 Mound structure and stratigraphy

Visible layering is common but not universal in mound deposits. It is picked out by reflectivity contrasts, probably due to differences in dust and/or frost concentration, or different resistance to erosion. Layers intersect the mound surface, forming contours on the gentle surface slopes, and outcrop geometries suggest that layering persists at depth within the mounds. We have mapped and measured spacing between layers on six crater mounds, three with partial dune cover and three without cover (Fig. 7). In addition, we have observed, (but did not measure) layers in mounds in craters 697, 795, 544 and 577 located in close proximity to the polar cap. Layers were not observed in craters 934, 904, 882 814, 811 and 480, where mounds are entirely covered by dunes. Crater 515 has no dunes, but no layers were observed, as in crater 436 which has partial dune cover. We have also found layering in a small mound in crater 332 (Fig. 2), which was excluded from our survey, because the mound does not have sufficient relief (> 150 m) to allow us to reliably distinguish it from a dunefield, a criteria set out in our mound identification in Section 2.1.

Interior layering of mounds is exposed in areas with erosion. These areas are systematically positioned on the south and east facing slopes of mounds (Fig. 7) and usually on the steeper

than average slopes. These zones spatially overlap with significant proportions of water ice in Fig. 6, in particular zones with water ice band depth > 0.7 water ice in Korolev (206), Dokka (388) and crater 579. This strongly suggests water ice is the principal component in the subsurface. We have estimated the thickness of 1438 layers in the six crater mounds with extensive exposures. Where CTX images were used, HiRISE images within the same scene were used to confirm that layers thinner than those easily visible in the CTX images were not present. Layer thickness ranged from 0.007 to 12 m, with an average of 0.42 m and a standard deviation of 1.55 m (Fig. 8). The layering observed in HiRISE images of the mound in Louth crater (503) is much finer than in all other mounds (median 0.15 m). In all cases apart from the fine-scale layering in Louth crater (503) layers are laterally continuous on scales of 100-1000 m.

Dips and strikes of layers were measured at 35 locations within mounds with extensive exposures (Fig. 7). Measured dips range up to 20° with a mean of ~ 5°. This is consistent with the distribution of surface slopes at sites with layer exposures (Fig. 9), with a mean of 4.4° and a maximum of about 20°. The difference between layer dip angles and surface slope at any given location ranges from 0 to 9°, with a mean of 2° and little skewing. This implies that the dip of the layers could be explained by draping of a topography similar to that of the present day outcrop sites. Figure 10 shows a detailed example of the interaction of layers with topography, highlighting that the dip directions are robust, even if the measured angles are subject to uncertainty (see Section 2.3 for a detailed discussion). The patterns of layer orientation are similar in all the mounds: strike orientations are similar to those of the present surface with dip directions away from the top of the mound and in some cases sub-parallel to crater-rim interior slopes. In all mounds with extensive exposures, layering is disrupted by unconformities. As an example, Fig. 10 shows unconformities observed within the mound in crater 579. Younging of these deposits towards the top of the mound can be inferred from the truncation of layers that are located stratigraphically below truncating layers (e.g., layer packet A (below) is truncated by layer packet B (above) in Fig.

10). Unconformities were also observed in Louth crater (503) with the same apparent trend. Although the younging directions are similar for coarse and fine-scale layering in this crater, exposures of the two layer types are separate. Hence, we cannot tell if the fine layered deposits are located stratigraphically beneath (i.e. older), or above (i.e. younger) the coarse layered deposits. The fine-scale layers in Louth (503) pinch out laterally on the scale of meters and have frequent discontinuities, which we interpret as evidence of small-scale topographic drape. Recent wind erosion of these layer outcrops has caused the formation of sharp, irregular groves or sastrugi (previously noted by Brown et al., 2008), draping of which would give rise to the observed stratigraphy.

SHARAD radar data shows that the layered structure of mound deposits extends deeper into the subsurface. We have found internal structures in the mounds of Korolev (206) and Dokka (388) craters. Verified with clutter simulations, radargrams of the interiors of these craters (e.g., Fig. 11) indicate that the main stratigraphy follows the contours of the present-day mounds. Layer thinning is observed on the gently dipping south facing slope in Korolev (Fig. 11). Layers deeper in the mound interior have a lower dip for both craters, but are more undulating in the case of Korolev. The following vertical measurements are directly dependent on the assumed permittivity, as we have chosen pure water ice they are maximum estimates (lower water ice contents would give reduced lengths). The minimum spacing between reflectors in the radargram for Korolev is estimated to be 6-18 m with approximately ~ 20 distinct reflectors visible over a thickness of ~ 2.5 km. The reflectors picked up by radar instruments, such as SHARAD are generally acknowledged to delineate packets of layers (Phillips et al., 2008; Putzig et al., 2009), rather than individual beds. The last return corresponds to ~ 3.9 km below the rim for Korolev, which compares favorably to the estimated depth of ~ 2.9 km from the relationships of Garvin et al. (2000) and 3.1 km from our results, implying that the permittivity of the mound material does not differ much from that of water ice, as was assumed in the depth correction. Thus, the SHARAD data

429 confirms that layering continues throughout the mound, and that the layered material is likely
430 to consist mainly of water ice over the entire depth of fill.

431 Other, smaller crater mounds did not produce internal radar reflections, probably because
432 they do not contain sufficiently continuous layering or sufficiently strong dielectric contrasts.
433 In the along and across track directions reflectors must be at least 300-1000 m and 1500-
434 8000 m long, respectively, to produce a strong radar return (Alberti et al., 2007). The mound
435 in crater 579 is likely to be sufficiently large to allow radar detection of internal structures, but
436 it had no SHARAD coverage, at the time of writing.

437 Given that layering appears to be pervasive within the mound deposits, we can surmise that
438 mound patches without exposed layering in Fig. 7 represent areas with present-day
439 deposition of water ice.

440 4. The origin and evolution of the crater-mounds

441 Eleven, possibly eighteen intermediate and large impact craters at high northern latitudes on
442 Mars have interior mounds consisting mainly of water ice. These ice-filled craters are some
443 of the deepest depressions in their surroundings. The mounds have a smooth, convex-up
444 shape, often asymmetrically placed within their crater and inclined to the south, surrounded
445 by a distinct moat. They have internal layering with unconformities indicating upward
446 younging of deposits and an alternation of phases of deposition and erosion. Layers appear
447 to drape over the extant topography of the mounds. This layering may be pervasive down to
448 the base of the deposits where they rest on the crater floor. Any explanation of the origin
449 and evolution of the crater mounds must address these key features. In this section we
450 consider four distinct scenarios of mound formation after a brief exploration of controls on
451 the present day geometry of the mounds.

4.1 Present-day form

The surface form and position of the mounds inside the craters may be determined by the mechanism that drives mound formation, or it could be due to subsequent processes changing the initial shape of the deposit. Only in the former case does the mound geometry contain information about the formative mechanism. Therefore we consider briefly whether post-depositional erosion alone can account for the mound shape. Using a radiation balance approach, and including effects of shadowing caused by the crater walls, atmospheric scattering, temperature-dependent re-radiation from the surface and conduction, Russell et al. (2004) have demonstrated that a north-south asymmetry and an exterior moat can be developed from an initially flat ice body inside a crater over limited time under current orbital configuration. They showed that any east-west asymmetry cannot be produced from radiation alone, but could be explained by aeolian processes, as winds coming off the cap are deflected longitudinally by planetary vorticity. Figure 12 shows the asymmetrical placement of the mounds within our studied craters. Mounds proximal to the cap have a westward displacement from the crater center and this matches the prevailing easterly wind direction as indicated by dune slip faces (Tanaka and Hayward, 2008). Mounds closer to the cap tend to be more asymmetric than those further away. These observations suggest that these mounds are primarily shaped by the wind, which is known to be stronger near the cap (e.g., Howard, 2000). Further away from the cap the mounds are placed obliquely or orthogonal to the prevailing wind, suggesting a stronger influence of radiation. The orientation of mound patches with exposures of internal layering in six of the craters (Fig. 7) matches this explanation. Dominance of south-facing layer exposures can be attributed to directionality of incident radiation, and east- or west-facing exposures can be related to regional winds. Together the asymmetry of the mounds and the orientation of layer exposures suggest that radiation-driven ablation and wind work together (with different relative magnitudes) to shape the existing ice deposits. This likely obviates the need to

478 invoke a primary formation mechanism to explain the present-day large-scale morphology of
479 crater mounds.

480 4.2 Remnant of a more extensive polar cap

481 As a first possible scenario of mound formation it has been proposed that the interior mound
482 of Korolev and similar features elsewhere could be erosional remnants of a formerly more
483 extensive polar cap (Fishbaugh and Head, 2000; Garvin et al., 2000; Tanaka et al., 2008),
484 along with outliers such as Olympia Mensae. Specifically, Tanaka et al. (2008) have
485 suggested that the Korolev deposit and those similar to it could be related to stratigraphic
486 unit "ABb1", the Polar Layered Deposits (PLD). A previously larger extent of the cap
487 (including the PLD and the Basal Unit beneath) is surmised based on the large erosional
488 scarps at the current margins of the cap, however the precise spatial extent is not known.
489 With reference to the position of outliers, Fishbaugh and Head (2000) and Johnson et al.
490 (2000) have proposed that the cap extended symmetrically down to 80-75°N. Rodríguez et
491 al. (2010) have argued that an extension of the PLD down to ~ 60°N and subsequent retreat
492 could account for the distribution of Late Amazonian pedestal craters. If the polar cap was
493 more extensive, then there is general agreement that it must have occurred under higher
494 obliquity conditions than at present (which favors migration of ice to lower latitudes), but the
495 exact timing is debated.

496 The PLD was laid down in the Amazonian as sub-horizontal layers from regular (possibly
497 seasonal) cycles of atmospheric deposition of water-ice mixed with small and variable
498 amounts of dust, producing regularly spaced layers with differing albedo of meter to tens of
499 meters in thickness. Layers are extremely laterally continuous (e.g., Fishbaugh and
500 Hvidberg, 2006) and angular unconformities occur mainly in association with the spiral
501 troughs (Putzig et al., 2009; Smith and Holt, 2010; Tanaka et al., 2008). These layers are
502 observed to generally dip at less than 1° from image (Milkovich et al., 2008) and SHARAD
503 radar data. Even layers draping trough walls do not have dips in excess of 1° (e.g. Fig. 3e of

Smith and Holt, 2010). The maximum total deposit thickness is estimated to be 1800 m from MARSIS radar data (Selvans et al., 2010). These deposits are thought to provide a record of past climate, similar to the polar ice caps on Earth (e.g., Cutts 1973; Laskar et al., 2002; Milkovich and Head, 2005; Milkovich et al., 2008). Estimates of past accumulation rates are on the order of 0.5 mm/yr (e.g., Laskar et al., 2002), or lower (Perron and Huybers, 2009). The modern polar cap is undergoing both accumulation, as shown by the burial of craters in fine-grained ice (Banks et al., 2010) and the lack of dust accumulation on its surface, and erosion, as shown by the exposure of coarser grained ice with lower albedo at scarps (Langevin et al., 2005).

Underlying a large part of the PLD is the Basal Unit (BU) or Planum Boreum Cavi unit (ABbc) using the nomenclature of Tanaka et al. (2008). This unit is characterized by a lower albedo compared to the PLD and is inferred to be rich in sandy material containing a variable quantity of volatiles. Layers have variable regularity and cross-bedding and a thickness up to decameters (Herkenhoff et al., 2007). Layers can be laterally discontinuous particularly on the 100 m scale with frequent angular unconformities. Lighter-toned layers are more resistant and thought to be more ice-rich. The BU is hypothesized to be of Middle to Late Amazonian age, originating from aeolian deposition, sometimes in the form of ice-cemented dunes. The dip angle of these layers has not been measured, but cross-bedded layers are locally steeper than strata of the PLD. The maximum deposit thickness is estimated to be 1100 m from MARSIS data (Selvans et al., 2010). It is possible that the BU, like the PLD has been more extensive in the past.

If the mounds in our study are remnants of a larger, continuous polar deposit then they might be expected to have a similar stratigraphy. Measured layer thicknesses on the mounds are generally within the range reported for the PLD (Milkovich et al., 2008). According to our own assessments of ~ 350 layers over three outcrops (see Section 2.3 for details) the PLD have layer spacing of 0.5 to 40 m with a median of 4.7 m and BU between 0.05 and 7.0 m with a

530 median of 1.4 m, presenting no statistically significant difference with layering in crater
531 mound deposits (Fig. 8). The only exception is the fine-scale layering found in the central
532 part of the mound in Louth crater (503), which is significantly and consistently finer than
533 layers measured anywhere else. However, the frequency of discontinuities (e.g. Fig 10) in
534 the mounds in general seems to be greater than within the PLD (where they are rare).This
535 implies that the mounds have experienced more erosive episodes. In addition, mound
536 layering is laterally less continuous, but this could be due to limited exposure compared to
537 the polar cap. Layer dip angles in the mounds are up to 20°, which is much greater than the
538 ~1° dips measured by Milkovich et al. (2008) for the PLD. Moreover, it would be expected in
539 the case of PLD-like deposition that layers should drape the crater walls, dipping gently
540 towards the center of the crater, with a flat lying central part as observed for craters
541 emerging from the polar cap (see Fig. 4 of Rodríguez et al., 2010). This contrasts with the
542 observed outward dip of mound layers that extends into the mound interior, indicating growth
543 from a central core (Figs. 7, 11).

544 Preservation of the mounds in crater interiors during cap-retreat has been attributed to the
545 shielding effect of the crater geometry (Garvin et al., 2000). For a given crater
546 depth/diameter ratio, then, the ice preservation rate should depend to a degree on the
547 radiation regime which changes with latitude. Confirmation of this link comes from the south
548 polar region, where the volume of ice bodies inside craters has been observed to decrease
549 away from the pole (Russell et al., 2003). However, there exists no such relationship either
550 between the mound volume as a proportion of the total cavity volume (a least squares linear
551 fit gives R^2 of 0.302 and p-value of 0.011), or the absolute mound volume and distance from
552 the polar cap in the northern hemisphere (R^2 of 0.058 and p-value of 0.806). This could
553 indicate a) a different origin for the mounds in the south compared to the north, or b) different
554 environmental factors determining mound survival between the two hemispheres (e.g.,
555 geometric shielding is less important than, for example, wind patterns in the north).

556 On balance we feel that stratigraphic, structural and volumetric evidence are not compatible
557 with the theory that crater mounds distal from the current polar cap formed as part of a larger
558 contiguous PLD or BU deposit. In particular this applies to Louth (503), Dokka (388), Korolev
559 (206), craters 579, 663 769 and 436, but we cannot rule out the role of a slightly more
560 extensive polar cap in the formation of mounds located proximal to the present-day polar cap
561 deposits.

562 4.3 Impact-driven water release

563 Our second scenario involves the mobilization of water from permafrost. It has been
564 hypothesized that relatively long-lived hydrothermal systems could be driven by the heat
565 released by a meteorite impact (Abramov and Kring, 2005; Osinski et al., 2005; Rathbun and
566 Squyres, 2002), or that the seismic energy of an impact can mobilize water/permafrost
567 (Harrison et al., 2010). This mechanism was suggested for the formation of a channeled
568 scabland extending from the ejecta blanket of Lyot crater located at 55°N, 330°W and a
569 band of paleo crater lakes (El Maarry, et al., 2010), both south of our study area. The
570 northern plains region of Mars should be particularly susceptible to the mobilization of
571 ground ice as it is abundant in the shallow sub-surface. The possibility of impact-induced
572 hydrothermal systems in permafrost-rich ground on Mars was first suggested by Brakenridge
573 et al. (1985). In this process the impact melt sheet of larger impact craters contains sufficient
574 heat energy to melt the surrounding permafrost and water contained in topographic highs
575 drains into the crater hollow. The resulting lake freezes at the surface, retarding evaporative
576 loss. Additional water can be sourced from subsequent hydrothermal circulation, driven by
577 temperature gradients within the surrounding regolith, which draws water into the crater
578 interior. Once the system has cooled sufficiently water starts to drain downwards out of the
579 crater lake and eventually a frost front may propagate upwards from the subsurface, leaving
580 a solid body of ice in the crater interior.

581 Rathbun and Squyres (2002) have shown that impacts creating craters with a diameter less
582 than 7 km have insufficient energy to sustain a crater lake. This cut off is relatively close to
583 the observed lower diameter limit for craters with mounds of ~ 9.5 km. For larger craters, the
584 presence or absence of a mound should then depend on the time since impact, and we
585 would expect to find mounds preferentially in the youngest craters. At received cratering
586 rates (e.g., Hartmann and Neukum, 2000), over our study area (excluding the area of the
587 cap), an impact such as Dokka (51 km diameter) could be as old as several hundreds of
588 millions of years and Korolev (80 km) over 1 Ga. It is unlikely that relatively small ice bodies
589 would have survived for this length of time, especially given that the polar cap is believed to
590 be no older than 4-5 Ma (e.g. Levrard et al., 2007). There are not sufficient craters in this
591 size range without a mound to confirm, or refute the impact heat theory, although we note
592 that Lyot crater, a large, 215 km diameter crater just south of our study area, has no
593 evidence of water ponding in its interior either as a mound, or a desiccated lake (Harrison et
594 al., 2010; Russell and Head, 2002).

595 In this scenario mound size should have no particular spatial trend, assuming that the same
596 amount of sub-surface water is available throughout the polar region, but depend primarily
597 on the energy of impact. As crater diameter is a proxy for impact energy, we might expect it
598 to scale with the mound volume (an approximation of the amount of water released).
599 Although the percent of the crater cavity in-filled by the mound does not correlate well with
600 the diameter of the crater, the absolute volume of infill increases with the crater diameter,
601 apparently as a power law with the form $(0.04\pm0.09)\ D^{2.8\pm0.2}$ with an R^2 of 0.983 and a p-
602 value of 9.6×10^{-11} where the uncertainty attached to the estimation of mound volume has
603 not been taken into account. However, the hydrothermal system is unlikely to have sustained
604 a hydraulic head permitting significant flow above the plains surrounding impact craters. In
605 fact, Rathbun and Squyres (2002) estimated a lake depth of 300 m for a 7 km diameter
606 crater and of ~ 1 km for a 180 km diameter crater (which is almost twice the diameter of
607 Korolev 206). Several craters in our survey have mounds that significantly exceed these

608 values. Additional elevation of the mounds (of up to 0.5-0.8 km in some cases) would have
609 to be accounted for, for example by invoking frost-heaving processes active in the waning
610 period of hydrothermal activity, similar to pingo formation on Earth, as suggested by
611 Sakimoto et al. (2005) and Bacastow and Sakimoto (2006).

612 It is perhaps most difficult to reconcile our observations of mound deposit stratigraphy with
613 the requirements of the scenario of impact-driven water release. Creation of the mounds by
614 this mechanism implies that the mounds have geologically the same age as the impact that
615 created their host crater, and are formed in a single event. Moreover, the mechanism could
616 give rise to complex, out-of-sequence layering as periods of hydrothermal injection into an
617 ice covered lake should cause under-plating and thermal erosion, similar to that of aufeis
618 (Gillespie et al., 2005). This could be followed by freezing of the water from both the top and
619 the bottom, producing frost-heave features, folding and faulting when the hydrothermal
620 system wanes. Water circulated through the subsurface at high temperatures may also
621 contain impurities consisting of salt and sediment that could be frozen into the deposits.
622 These expected characteristics contrast with our observation of regular, upward younging
623 layers of relatively pure ice, without major faults, or folds. In Louth crater (503) small-scale
624 layering has more folds, but is still relatively regular. Finally, the pervasive presence of large-
625 scale discontinuities in the mound deposits suggests an evolution involving multiple events.
626 This, and lack of correspondence with proposed crater lake dimensions are all problems for
627 this mechanism.

628 4.4 Artesian flow

629 The third scenario of mound formation appeals to the presence of deep-seated faults below
630 impact craters (e.g., Christeson et al., 2001). These faults could tap into a deep aquifer
631 confined by the cryosphere that is hypothesized to underlie the north polar plains (as
632 predicted by Clifford, 1993; Clifford and Parker, 2001; Clifford et al., 2010), providing a
633 conduit to the surface for the confined water. Water would come to the surface at times

634 when the cryosphere enlarges and impinges on the aquifer producing sufficient confining
635 pressure. This mechanism has been proposed for the creation of crater lakes at lower
636 latitudes by Newsom et al. (1996). Upwellings would not necessarily occur at the same time
637 as the impact event and could occur many times, producing a layered stratigraphy as
638 observed. Assuming that the top of the aquifer is located on a single level, then mounds
639 should be found in large craters with large fault systems, but also smaller craters located on
640 low-lying topography. Our results show this trend, where mounds are found in craters which
641 tend to penetrate to the deepest local elevation (Fig. 4). If the aquifer is fully connected and
642 the mounds formed at the same time then the mounds should extend up to a similar
643 topographic elevation, equal to the hydraulic head. This is not the case. If flow rates are low,
644 then it might be expected that smaller mounds should be found in craters with a base
645 located at higher absolute elevation. We do observe a very weak negative relationship
646 between the inferred elevation of the crater base and both relative (linear) and absolute
647 mound volume (exponential), with R^2 values of 0.006 and 0.37 respectively and p-values of
648 0.31 and 0.003 respectively.

649 As in the hydrothermal hypothesis mound formation would involve processes akin to those
650 occurring in pingos. This, together with wind and/or radiation ablation could give rise to
651 doming of the mounds. The internal stratigraphy of such mounds should be complex. Water
652 could pond on the surface and gradually freeze as a lake system, or could inject underneath
653 pre-existing ice. Subsequent pulses would deform, fracture and fold, possibly under-plating
654 the roof, or breaking through to the surface, filling topographic hollows. Potentially the age of
655 the ice could increase, or decrease towards the center, depending on the dominant
656 emplacement mechanism. Ice interior to the mounds should have many discontinuities, folds
657 and faults. Such complexity is not characteristic of the mounds in our study, which display
658 regular layering, large-scale discontinuities, minor folding and no faulting. The fine-scale
659 layering in Louth crater (503) is the only example that shows sufficient complexity to fit with
660 this model, but it is the exception, rather than the rule. Interestingly, the mound in that crater

661 is placed very eccentrically, as would be expected from the peripheral position of impact fault
662 systems. However, neither there nor elsewhere have we found spectroscopic evidence for
663 the presence of salts in mound deposits, which is expected for upwelling water sourced at
664 depth. In addition, there appears to be a discrepancy between the observed distribution of
665 crater mounds and the geometry of the putative deep aquifer (Clifford, 1993). The aquifer is
666 thought to be located deepest close to the polar cap, where surface temperatures are
667 lowest, but there we have found mounds in several craters of limited diameter and depth. It
668 is possible that the aquifer is located at shallower depths than proposed by Clifford (1993)
669 very near to the pole, due to water being supplied from the base of the polar cap (e.g.,
670 Longhi, 2006). Away from the polar cap, the cryosphere is thought to thin southward, making
671 mound or lake formation more likely in this scenario. The lack of evidence for hydrological
672 activity in Lyot crater (Russell and Head, 2002; Harrison et al., 2010) is at odds with this
673 expectation. Despite the mounds occurring in the deeper penetrating circumpolar craters,
674 inconsistencies in stratigraphy, composition, position and distribution argue against artesian
675 flow from a deep aquifer as a formative mechanism for these mounds.

676 4.5 Crater microclimate

677 Our fourth hypothesis calls on microclimate phenomena associated with crater topography
678 for growth of ice mounds from atmospheric deposition. We start our exploration of this
679 mechanism with some observations of temperature and albedo in and around craters in the
680 north polar region.

681 4.5.1 Craters as cold traps

682 The temperature and albedo evolution of ice mounds in Korolev and Dokka through the
683 Martian year have been reported by Armstrong et al. (2005) and Kuti (2009). These mounds
684 are consistently ~ 10 K cooler than ice-free terrain at the same latitude for most of the year,
685 with an accentuated daytime difference of ~20-40 K in summer months (Fig. 13). On these

686 crater mounds, surface temperatures remains close to the water frost point throughout the
687 year (particularly at night). In other craters without ice (an example is given in Fig. 13),
688 temperatures inside and outside the craters are very similar for most of the year. These
689 observations suggest that the presence of ice modulates local near surface temperatures in
690 crater interiors. A minimum thickness of ice of several meters at the surface may be required
691 to produce this effect (Armstrong et al., 2005). So how did this initial ice layer come about in
692 the craters with mounds, and how and when does/did this volatile deposition occur?
693 The following thermal, spectral and image data reveal that crater cavities may enhance the
694 deposition and/or preservation of volatiles at the present day. Viking Infrared Thermal
695 Mapper (Kieffer 1977) and Thermal Emission Spectrometer (TES; Titus et al. 2001)
696 observations have shown temperatures below the CO_2 sublimation point inside craters
697 during winter. These cold spots are unlikely to represent real surface temperatures, but
698 could be caused by cloud formation and thus possibly increased deposition of CO_2 ice
699 (Ivanov and Muhleman, 1999). In agreement with these observations, we also observe that
700 apparent crater floor temperatures with and without ice mounds are up to 10°K below those
701 outside the crater between L_s = 240-320° (Fig. 13).

702 We have examined published OMEGA data (Appéré et al., 2011) and HiRISE and CTX
703 images for presence of surface ice at latitudes greater than 60°N around the L_s = 60° crocus
704 date, when CO_2 frost is receding. The OMEGA data show that crater floors remain covered
705 in water ice for approximately 5° of L_s after the main seasonal cap has retreated to higher
706 latitudes (Figures 5-8 Appéré et al., 2011). These deposits then degrade to an annulus
707 around the crater rim, before disappearing. HiRISE and CTX images show that crater floors
708 rarely have any remnant high albedo ice deposits after the crocus date. They do show,
709 however, that high albedo patches remain after the crocus date on north-facing crater slopes
710 (Fig. 14B) and sometimes as E-W 'plumes' outside the crater (Fig. 14A). Many of these
711 patches disappear in the summer, but some remain as shown in CRISM analyses performed
712 by Seelos et al. (2008). These authors have hypothesized that the 'plumes' are a result of

713 wind-driven, orographic deposition of water ice. Hajigholi et al. (2010) monitored seven
714 craters at > 55°N and also noted crater interiors were favored sites for ice deposition. These
715 observations show that crater floors are not presently sequestering H_2O or CO_2 deposited in
716 the seasonal polar cap under present day conditions.

717 If atmospheric deposition is the driving process in which layers are constructed, then to start
718 mound formation, ice build-up in winter months on the crater floor must outstrip sublimation
719 in spring and summer. The presence of high-albedo ice deposits throughout the year may
720 then locally suppress near surface temperatures and form a long-lived cold trap for H_2O. It is
721 possible that the ice layer needed to trigger further build-up is provided by a hydrothermally
722 induced crater lake, or the remnant of a more extensive cap deposit. Below, we examine a
723 scenario that does not involve an external start, and is instead entirely climate-driven.

724 4.5.2 Reduced sublimation of water ice in craters

725 We have demonstrated that at least seasonally all craters trap water ice. However, this does
726 not explain why only some craters in the near polar area host mounds and why others do
727 not. We suggest that this is because of differing preservation potentials between the craters,
728 which are determined by differing rates of sublimation. Factors, such as shadowing within
729 the crater, differences in surface thermophysical properties, atmospheric temperature,
730 atmospheric pressure and the wind regime, play a role in defining the sublimation rate.

731 The higher the surface temperature the more rapid the sublimation, so cooler temperatures
732 favor the preservation of ice mounds. The surface temperature is controlled by insolation
733 (and thus shading) and surface themophysical properties. If we consider shadowing alone,
734 water ice should be preserved on all north-facing crater walls rather than on crater floors and
735 mounds should therefore have an off-center nucleus, positioned on the north-facing slope. In
736 the craters where we have studied the stratigraphy the nucleus of the mound is located on
737 the crater floor and not all craters have mounds, hence this factor alone does not explain our

738 observations. We cannot determine the surface material albedo and thermal inertia of the
739 craters prior to mound deposition; hence we cannot definitively say what role these
740 thermophysical properties played.

741 The atmospheric pressure at the base of a crater is greater than on the surrounding plains
742 (due to altitude) and this can act to reduce sublimation by free convection (e.g., Ingersoll,
743 1970). As the mounds are often found in craters that penetrate deeply into the crust (Fig. 4),
744 this may be one factor that could help to explain the mound distribution. However, other
745 factors must be playing a role, because not all deeply penetrating craters have mounds.
746 Wind speed and its saturation level also play a key role in sublimation, with strong, dry winds
747 enhancing forced sublimation (e.g., Ingersoll, 1970). Given this, it might be expected that
748 craters with mounds should be located away from the strong summer katabatic winds, but
749 we observe no systematic placement of craters with mounds with respect to these winds
750 (see maps in Massé et al. 2012, Ewing et al., 2010 and Howard, 2000). At a smaller scale
751 craters generate their own wind systems. Fenton and Hayward (2010) noted a peculiar
752 “bullseye” dunefield morphology in craters close to the southern polar cap, and attributed it
753 to inward flowing local katabatic winds. We see the same morphology inside many of the
754 craters with mounds and inside other craters in the area, indicating the strong influence of
755 local winds. The topography of each crater would have different effects on these wind
756 patterns, but with the data available we find no systematic pattern to explain why some
757 craters have mounds and others do not. To precisely determine the role of local-scale winds
758 in triggering mound formation would require a full meso-scale climate model (e.g. Spiga, et
759 al. 2011), which is outside the scope of this paper.

760 ### 4.5.3 Initiation and mound building

761 We envisage the following sequence of events (Fig. 15) for the initiation and evolution of
762 mound building:

763 1) In winter condensation of water ice is followed by the condensation of CO_2 intermixed with
764 a smaller fraction of water ice. The micoenvironment inside the crater interior causes
765 additional condensation of volatiles over the winter period, resulting in a thicker layer of both
766 CO_2 and H_2O in the crater floor than on surrounding plains.
767 2) The CO_2 layer is first to sublimate in spring. This process is driven by direct insolation, but
768 also draws heat from the surrounding atmosphere, and this maintains a low temperature in
769 the crater interiors (~150 K). Simultaneously, water ice is sublimating at lower latitudes and
770 this water vapor can condense back on to the sublimating CO_2 deposits at higher latitudes
771 (e.g. Appéré et al. 2011). The thicker layer of CO_2 deposited on the crater floor, and lower
772 local temperatures cause the crater floor to defrost later than the surrounding landscape.
773 This means that the process of re-condensation of water vapor can continue for longer and
774 in particular while H_2O is sublimating from the landscape immediately surrounding the crater.
775 3) Once the surrounding landscape has completely defrosted and the CO_2 sublimation in the
776 crater has finished, there remains a layer of water ice condensed over winter and additional,
777 re-condensed water ice layer.
778 4) The sublimation of this remaining water ice is retarded by the microclimate of the crater
779 interior (likely pressure and wind effects). Due to the high albedo of the deposit both free and
780 forced sublimation will also be slowed due to the lower atmospheric temperature above the
781 deposit (further enhanced if the deposit is thick). A thick layer (with high thermal inertia)
782 might permit re-condensation during the night if any sublimation has occurred.
783 5) Once a “thick” layer has been built (~1-4 m required according to Armstrong et al., 2005)
784 this creates a positive feedback, whereby the high albedo and high thermal inertia form a
785 cold trap which produces net accumulation over the course of a year (Fig. 13). Then, water
786 vapor delivered to the crater at almost any time of year could freeze onto the existing
787 deposit, and progressive build-up of an ice mound would ensue.
788 Atmospheric deposition would give rise to upward younging stratigraphy, with regular
789 layering, reflecting cyclical deposition on seasonal, but more likely much longer timescales.

Changes in the balance of deposition and ablation could cause alternation of aggradation and decay of the deposits, recorded in (angular) unconformities within the mound stratigraphy. During an initial build up phase, deposits are expected to line the crater interior, but solar irradiation and directional ablation by winds would eventually cause the formation of a moat and give the deposit a characteristic mound shape. Further volatile deposition would drape the mound topography, dipping outward from an accumulation center, and following any erosional detail in the pre-existing ice surface. All of these expectations are matched by our stratigraphic observations.

4.5.4 Timing

At present, craters are not initiation points for mound building, nor is mound building very rapid. Assuming that current maximum deposition rates are similar to those on the north polar cap, 3-4 mm/yr (Banks et al., 2010), a mound such as the one in Korolev would take ~ 500 ka to form when deposition is uninterrupted. Orbital forcing of climate is important on this time scale. Using a global climate model and different orbital parameters Levrard et al. (2007) showed that obliquity (axial tilt, ~124 ka cycle) is the primary orbital control on ice accumulation in the polar region. Low obliquity favors polar cap accumulation and obliquities greater than 30° can destabilize ice in the whole polar region (which last occurred at ~0.4 Ma). Another important feature is the precession cycle (~51 ka), a combined effect of the eccentricity and longitude of the perihelion. The orbit of Mars is elliptical, so that northern hemisphere spring is the longest season, followed by northern summer, winter and the shortest season is autumn, the present-day location of the perihelion. Thus, northern winters are comparatively short and warm, and summers are long and cool. If the perihelion is located in northern summer, then winters become longer cooler and the summer becomes short and relatively hot. It is the length of the seasons, rather than their relative temperature, that governs ice accumulation at obliquities less than 25° (Levrard et al., 2004; Levrard et al., 2007). As the obliquity has been relatively stable over the last 500 ka, precession cycles

816 dominate. We suggest that mound triggering and building may be favored when the
817 perihelion is located in summer or autumn, allowing a longer period of winter deposition and
818 a long spring period when volatiles are delivered from the receding seasonal cap and the
819 main polar deposits. This situation last occurred between 10-25 ka before present
820 (Montmessin et al., 2007). These cycles could account for the large angular unconformities
821 that we observe. Further modeling is required to accurately ascertain orbital parameters that
822 are favorable to mound building.

823 If the mounds are indeed formed by atmospheric deposition, then their overall form and
824 internal stratigraphy are controlled by climatic conditions. If their timescale of adjustment is
825 relatively quick compared to the timescale of climate change then they should provide a
826 stratigraphic record of recent climate changes, driven by changes in Mars' orbital
827 configuration.

828 ### 4.5.5 Other ice outliers

829 We surveyed the outlying high albedo deposits that are not located within craters to
830 ascertain if there was a common formation mechanism with the mounds inside craters. The
831 majority of these deposits are mostly thin (they show underlying impact craters of ~ 500 m
832 diameter with an expected rim height of ~ 25 m) and only around Olympia Mensae (between
833 ~95-135°E and ~73-80°N, Fig. 2, marked "OM") do they reach thicknesses of > 100 m. The
834 presence of relatively thin outliers located between Dokka, Korolev and the Olympia Undae
835 dunefield (between ~150-240°E and ~75-80°N latitude) has been previously attributed to the
836 presence of polar deposits underlying this area (Fishbaugh and Head, 2000). Tanaka et al.
837 (2008) classified these high albedo deposits as 'ABb_4' or Planum Boreum 4 unit, which is the
838 unit that caps the present polar cap, and suggested that these deposits are recent (last
839 21.5 ka) and relatively thin. Recent radar data has confirmed that the BU extends beneath
840 the Olympia Undae dunefield (Selvans et al., 2010), making it quite plausible that thin
841 deposits extend further north. These high albedo deposits occur where dunes are not

842 present, so it could be that they are accumulations resulting from the exposure and resulting
843 cold-trap effect of BU deposits.
844 The presence of thicker deposits in the Olympia Mensae area is more difficult to explain.
845 They occur as discrete patches with steep boundary scarps with up to ~20° slopes and
846 thickness of up to 350 m, but more generally around 100 m. They are located latitudinally
847 between and to the east of Louth (503) and crater 579. This area is of relatively high
848 elevation compared to the same latitude elsewhere around the pole. Three of the outcrops
849 are elongate in the E-W direction and have layer exposures in all orientations, consistent
850 with wind erosion rather than radiation as the primary shaping mechanism. The Olympia
851 Mensae deposits have visually very similar stratigraphy to the crater mounds in terms of
852 layer spacing and presence of low-angle unconformities, but only have very low dips (<1°)
853 and no draping layers (Fig. 16). They have almost 100 % exposure of the layers, which
854 implies they are currently undergoing retreat. This is supported by Brown et al. (2011), who
855 suggest that sublimation in the Olympae Mensae region might be the main source of the
856 water which masks the CO_2 seasonal cap during its spring regression. This suggests these
857 outliers unlike the crater mounds have not undergone significant recent deposition and
858 therefore their evolution is somewhat different to that of the ice mounds inside craters. The
859 questions of how their deposition was triggered and their previous extent are left open as
860 targets for future investigation.

861 5. Conclusions

862 We have identified and studied 18 inner-crater mounds in Mars' north polar region that have
863 an origin different from the central peaks normally found in complex craters. They are
864 restricted to craters with a diameter >9.5 km located at latitudes > 70°N. Two of these crater
865 mounds consist largely of water ice according to radar data and nine others have substantial
866 water ice at the surface as observed in spectral data. We infer by similarity of form and
867 location that the other mounds are also composed of water ice. Their large-scale

morphology, flat topped with a circumferential moat, can be explained by ablation of volatiles by solar radiation and wind, leaving no indication of the formation mechanism.

The formation of these mounds by either impact-induced hydrothermal circulation or artesian upwelling is inconsistent with the generally unfolded and unfaulted, regular layering with upward younging stratigraphy exposed on mound surfaces. Moreover, ice layers drape the existing topography on at least six of the mounds, implying growth from a central core. This is inconsistent with these mounds being erosional remnants of a previously more extensive polar cap. It is plausible that this form of growth is shared by eight other mounds that are not directly adjacent to the present polar cap. For the four mounds abutting the present polar cap we cannot rule out an origin by cap retreat.

Ice accumulations can be maintained or grow by cold trapping when they have attained a minimum thickness required to form a negative thermal anomaly that persists throughout the year. This minimum condition can be achieved in one of three ways: a frozen paleo-lake from an impact hydrothermal system, a remnant of a more extensive polar cap, or atmospheric deposition driven by microclimate processes inside the crater. We have no observational evidence to support any of these initiation mechanisms, but we have explored in more detail the possibility that mound formation is entirely due to the microclimatic characteristics of deep impact craters at high northern latitudes.

Mounds are found in deeply penetrating craters where atmospheric pressures are high compared to the areas surrounding the crater. This suppresses ice sublimation, but not all deeply penetrating craters have mounds, so other climatic factors, such as wind regime, must be playing a role. We suggest that microclimatic effects act to suppress the sublimation of seasonal ice in springtime, both increasing its lifetime and creating a cold-trap onto which volatiles released from the surrounding landscape during warm seasons can condense. It is likely that during periods when Mars' orbital perihelion was located in northern summer, longer winters have allowed enhanced deposition of volatiles, while the potential for sublimation was limited by the brevity of summers. Under these conditions, which last

occurred 10-25 ka ago, enough ice may have built up in deep crater interiors to start a positive feedback permitting mound building due to the formation of long lived cold trap above bodies with high albedo and thermal inertia. The main supply of water vapor to these cold traps may be the seasonal cap with secondary input from katabatic winds flowing from the polar cap during spring and early summer.

Where mound surfaces are not clad by dunes, the fact that layers are seen to be exposed at the surface indicates recent or ongoing erosion in these areas. However, elsewhere the lack of visible layering can be attributed to recent deposition of ice draping the mound topography. Hence, the mounds are currently undergoing change, likely driven by changes in the local climate. Changes in climate may shift and resize the depositional and erosion areas, explaining the complex pattern of discontinuities visible in exposed mound stratigraphy. If this interpretation is correct, then the crater mounds may be sensitive recorders of climate change in the north polar area, located in closest proximity to the main source of volatiles on present day Mars. Further investigation of their stratigraphy and dynamics may yield new insights into the past and present H_2O and CO_2 cycles of the planet.

Acknowledgements

Firstly we thank Colin Dundas and Adrian Brown for their thorough and thoughtful reviews, which greatly improved the manuscript. We thank Edwin Kite, Simon Dadson, and Dimitri Lague for their additions and critique. Additional support provided by the Earth Science Department at Cambridge University was essential in completing this work. We are indebted to the late Ali Safaeinili who created the code enabling estimation of the SHARAD time to depth conversion. Marion Massé provided useful discussion on CRISM and OMEGA spectral data. Many thanks to Rosalyn Hayward for giving permission to use her data on dunefields in the north polar region and Lori Fenton for useful discussion regarding bullseye dunes. Thomas Appéré provided insightful comments on polar seasonal processes.

References

Abramov, O., Kring, D. A., 2005. Impact-induced hydrothermal activity on early Mars. J. Geophys. Res. 110 (E12), doi:10.1029/2005je002453.

Alberti, G., Dinardo, S., Mattei, S., Papa , C., Santovito, M. R., 2007. SHARAD radar signal processing technique. IWAGPR 4th International Workshop on Advanced Ground Penetrating Radar, Naples, Italy.

Antoniadi, E. M., 1930. La Planète Mars. Herman, Paris.

Appéré, T., B. Schmitt, Y. Langevin, S. Douté, A. Pommerol, F. Forget, A. Spiga, B. Gondet, J. P. Bibring (2011), Winter and spring evolution of northern seasonal deposits on Mars from OMEGA on Mars Express, J. Geophys. Res. 116(E5), E05001, doi:10.1029/2010JE003762.

Armstrong, J. C., Titus, T. N., Kieffer, H. H., 2005. Evidence for subsurface water ice in Korolev crater, Mars. Icarus. 174 (2), 360-372.

Armstrong, J. C., Nielson, S. K., Titus, T. N., 2007. Survey of TES high albedo events in Mars' northern polar craters. Geophys. Res. Lett. 34, doi:10.1029/2006GL027960.

Bacastow, A. L., Sakimoto, S. E. H., 2006. Martian North Polar Crater Morphology: Implication for an Aquifer. Lunar Planet. Sci. 37. Abstract 2239.

Banks, M. E., Byrne, S., Galla, K., McEwen, A. S., Bray, V. J., Dundas, C. M., Fishbaugh, K. E., Herkenhoff, K. E., Murray, B. C., 2010. Crater population and resurfacing of the Martian north polar layered deposits. J. Geophys. Res. 115 (E8), doi:10.1029/2009JE003523.

942 Barlow, N. G., Perez, C. B., 2003. Martian impact crater ejecta morphologies as indicators of
943 the distribution of subsurface volatiles. J. Geophys. Res. Planets. 108 (E8),
944 doi:10.1029/2002JE002036.

945 Barnie, T. D., 2006. Placing constraints on the origin of the ice fill of north polar ice impact
946 craters on Mars using impact crater and ice fill morphology. Master's Thesis,
947 University of Aberystwyth, pp. 114.

948 Bibring, J. P., Langevin, Y., Gendrin, A., Gondet, B., Poulet, F., Berthe, M., Soufflot, A.,
949 Arvidson, R., Mangold, N., Mustard, J., Drossart, P., 2005. Mars surface diversity as
950 revealed by the OMEGA/Mars Express observations. Science 307 (5715), 1576-
951 1581.

952 Brakenridge, G. R., Newsom, H. E., Baker, V. R., 1985. Ancient hot springs on Mars: Origins
953 and paleoenvironmental significance of small Martian valleys. Geology 13 (12), 859-
954 862.

955 Brown, A. J., Byrne, S., Tornabene, L. L., Roush, T., 2008. Louth crater: Evolution of a
956 layered water ice mound. Icarus 196 (2), 433-445.

957 Brown, A. J., Calvin, W., 2010. MRO (CRISM/MARCI) Mapping of the North Pole - First
958 Mars Year of Observations. Lunar Planet. Sci. 41. Abstract 1278.

959 Brown, A. J., Calvin, W., McGuire, P., Murchie, S., 2010. Compact Reconnaissance Imaging
960 Spectrometer for Mars (CRISM) south polar mapping: First Mars year of
961 observations. J. Geophys. Res. Planets. 115, doi:10.1029/2009JE003333.

962 Brown, A. J., Calvin, W., Hollingsworth, J. L., Schaefer, J. R., Michaels, T. I., Mellem, B. A.,
963 2011. CRISM and MARCI Observations of North Polar Springtime Recession for MY
964 29/30. . Fifth International Conference on Mars Polar Science and Exploration
965 Abstract 6060.

966 Boyce, J.M., Mouginis-Mark, P., Garbeil, H., 2005. Ancient oceans in the northern lowlands
967 of Mars: Evidence from impact crater depth/diameter relationships. J.Geophys. Res.
968 110, doi:10.1029/2004JE002328.

969 Byrne, S., Dundas, C.M., Kennedy, M.R., Mellon, M.T., McEwen, A.S., Cull, S.C., Daubar,
970 I.J., Shean, D.E., Seelos, K.D., Murchie, S.L., Cantor, B.A., Arvidson, R.E., Edgett,
971 K.S., Reufer, A., Thomas, N., Harrison, T.N., Posiolova, L.V., Seelos, F.P., 2009.
972 Distribution of mid-latitude ground ice on mars from new impact craters. Science 325,
973 1674-1676.

974 Calvin, W. M., Roach, L. H., Seelos, F. P., Seelos, K. D., Green, R. O., Murchie, S. L.,
975 Mustard, J. F., 2009. Compact Reconnaissance Imaging Spectrometer for Mars
976 observations of northern Martian latitudes in summer. J. Geophys. Res. 114,
977 doi:10.1029/2009JE003348.

978 Christeson, G. L., Nakamura, Y., Buffler, R. T., Morgan, J., Warner, M., 2001. Deep crustal
979 structure of the Chicxulub impact crater. J. Geophys. Res. 106 (B10), 21751-21769.

980 Clifford, S. M., 1993. A Model for the Hydrologic and Climatic Behavior of Water on Mars. J.
981 Geophys. Res. Planets 98 (E6), 10973-11016.

982 Clifford, S. M., Parker, T. J., 2001. The evolution of the Martian hydrosphere: Implications for
983 the fate of a primordial ocean and the current state of the northern plains. Icarus 154
984 (1), 40-79.

985 Clifford, S. M., Lasue, J., Heggy, E., Boisson, J., McGovern, P., Max, M. D., 2010. Depth of
986 the Martian cryosphere: Revised estimates and implications for the existence and
987 detection of subpermafrost groundwater. J. Geophys. Res. 115 (E7),
988 doi:10.1029/2009JE003462.

989 Cull, S., Arvidson, R. E., Mellon, M., Wiseman, S., Clark, R., Titus, T., Morris, R. V.,
990 McGuire, P., 2010. Seasonal H_2O and CO_2 ice cycles at the Mars Phoenix landing
991 site: 1. Prelanding CRISM and HiRISE observations. J. Geophys. Res. 115,
992 doi:10.1029/2009JE003340.

993 Cutts, J.A., 1973.Nature and origin of layered deposits of the Martian polar regions. J.
994 Geophys. Res., 78, 4231–4249.

995 El Maarry, M. R., Markiewicz, W. J., Mellon, M. T., Goetz, W., Dohm, J. M., Pack, A., 2010.
996 Crater floor polygons: Desiccation patterns of ancient lakes on Mars? J. Geophys.
997 Res. 115 (E10), doi:10.1029/2010JE003609.

998 Ewing, R. C., Peyret, A.-P. B., Kocurek, G., Bourke, M., 2010. Dune field pattern formation
999 and recent transporting winds in the Olympia Undae Dune Field, north polar region of
1000 Mars. J. Geophys. Res. 115 (E8), doi:10.1029/2009JE003526.

1001 Feldman, W. C., Prettyman, T. H., Maurice, S., Plaut, J. J., Bish, D. L., Vaniman, D. T.,
1002 Mellon, M. T., Metzger, A. E., Squyres, S. W., Karunatillake, S., Boynton, W. V.,
1003 Elphic, R. C., Funsten, H. O., Lawrence, D. J., Tokar, R. L., 2004. Global distribution
1004 of near-surface hydrogen on Mars. J. Geophys. Res. 109 (E9),
1005 doi:10.1029/2003JE002160.

1006 Fenton, L.K., Hayward, R.K., 2010. Southern high latitude dune fields on Mars: Morphology,
1007 aeolian inactivity, and climate change. Geomorphology 121, 98-121.

1008 Fishbaugh, K. E., Head, J. W., 2000. North polar region of Mars: Topography of circumpolar
1009 deposits from Mars Orbiter Laser Altimeter (MOLA) data and evidence for
1010 asymmetric retreat of the polar cap. J. Geophys. Res. 105, 22455-22486.

1011 Fishbaugh, K. E., Hvidberg, C. S., 2006. Martian north polar layered deposits stratigraphy:
1012 Implications for accumulation rates and flow. J. Geophys. Res. 111 (E6),
1013 doi:10.1029/2005je002571.

1014 Garvin, J. B., Sakimoto, S. E. H., Frawley, J. J., Schnetzler, C., 2000. North Polar Region
1015 Craterforms on Mars: Geometric Characteristics from the Mars Orbiter Laser
1016 Altimeter. Icarus 144, 329-352.

1017 Garvin, J. B., 2005. Impact Craters on Mars: Natural 3D Exploration Probes of Geological
1018 Evolution. Workshop on the Role of Volatiles and Atmospheres on Martian Impact
1019 Craters. LPI Laurel, Maryland. Abstract 1273, p.38-39.

1020 Gillespie, A. R., Montgomery, D. R., Mushkin, A., 2005. Planetary science: Are there active
1021 glaciers on Mars? Nature. 438 (7069), E9-E10.

1022 Hajigholi, M., Bertilsson, S. A. M., Brown, A. J., McKay, C. P., Fredriksson, S., 2010.
1023 Monitoring Seasonal Behavior of Ices in the Craters in the Martian Northern Polar
1024 Region with CTX and HiRISE. Lunar Planet. Sci. 41. Abstract 1553.

1025 Harrison, T. N., Malin, M. C., Edgett, K. S., Shean, D. E., Kennedy, M. R., Lipkaman, L. J.,
1026 Cantor, B. A., Posiolova, L. V., 2010. Impact-induced overland fluid flow and
1027 channelized erosion at Lyot Crater, Mars. Geophys. Res. Lett. 37 (21),
1028 doi:10.1029/2010gl045074.

1029 Hartmann, W. K., Neukum, G., 2001. Cratering Chronology and the Evolution of Mars.
1030 Space Sci. Rev. 96, 165-194.

1031 Herkenhoff, K. E., Byrne, S., Russell, P. S., Fishbaugh, K. E., McEwen, A. S., 2007. Meter-
1032 Scale Morphology of the North Polar Region of Mars. Science 317 (5845), 1711-
1033 1715.

1034 Hovius, N., Conway, S. J., Barnie, T. D., Besserer, J., 2009. Ice Filled Craters in Mars' North
1035 Polar Region -- Implications for Sub-Surface Volatiles. Lunar Planet. Sci. 40. Abstract
1036 2042.

1037 Howard, A. D., 2000. The Role of Eolian Processes in Forming Surface Features of the
1038 Martian Polar Layered Deposits. Icarus 144 (2), 267-288.

1039 Ingersoll, A. P., 1970. Mars: Occurrence of liquid water. Science 168, 972-973.

1040 Ivanov, A. B., Muhleman, D. O., 2001. Cloud Reflection Observations: Results from the Mars
1041 Orbiter Laser Altimeter. Icarus 154 (1), 190-206.

1042 Jakosky, B. M., Mellon, M. T., Varnes, E. S., Feldman, W. C., Boynton, W. V., Haberle, R.
1043 M., 2005. Mars low-latitude neutron distribution: Possible remnant near-surface water
1044 ice and a mechanism for its recent emplacement. Icarus 175, 58-67.

1045 Johnson, C. L., Solomon, S. C., Head, J. W., Phillips, R. J., Smith, D. E., Zuber, M. T., 2000.
1046 Lithospheric Loading by the Northern Polar Cap on Mars. Icarus 144 (2), 313-328.

1047 Kieffer, H.H., Martin, T.Z., Peterfreund, A.R., Jakosky, B.M., Miner, E.D., Palluconi, F.D.,
1048 1977. Thermal and Albedo Mapping of Mars During the Viking Primary Mission. J.
1049 Geophys. Res. 82, 4249-4291, doi:10.1029/JS082i028p04249.

1050 Kreslavsky, M. A., Head, J. W., 2006. Modification of impact craters in the northern plains of
1051 Mars: Implications for Amazonian climate history. Meteorit. Planet. Sci. 41, 1633-
1052 1646.

1053 Kuti, A., 2009. Thermal Behavior of Dokka Crater and its Surroundings in the North Polar
1054 Region of Mars. Lunar Planet. Sci. 40. Abstract 1006.

1055 Langevin, Y., Poulet, F., Bibring, J. P., Gondet, B., 2005. Summer evolution of the north
1056 polar cap of Mars as observed by OMEGA/Mars express. Science. 307 (5715), 1581-
1057 1584.

1058 Laskar, J., Levrard, B., Mustard, J. F., 2002. Orbital forcing of the martian polar layered
1059 deposits. Nature 419 (6905), 375-377.

1060 Levrard, B., Forget, F., Montmessin, F., Laskar, J., 2004. Recent ice-rich deposits formed at
1061 high latitudes on Mars by sublimation of unstable equatorial ice during low obliquity.
1062 Nature 431 (7012), 1072-1075.

1063 Levrard, B., Forget, F., Montmessin, F., Laskar, J., 2007. Recent formation and evolution of
1064 northern Martian polar layered deposits as inferred from a Global Climate Model. J.
1065 Geophys. Res. 112 (E6), E06012.

1066 Levy, J., Head, J. W., Marchant, D. R., 2010. Concentric crater fill in the northern mid-
1067 latitudes of Mars: Formation processes and relationships to similar landforms of
1068 glacial origin. Icarus 209 (2), 390-404.

1069 Longhi, J., 2006. Phase equilibrium in the system CO_2-H_2O: Application to Mars. J.
1070 Geophys. Res. Planets. 111 (E6), doi:10.1029/2005JE002552.

1071 Massé, M., Bourgeois, O., Le Mouélic, S., Verpoorter, C., Spiga, A., Le Deit, L., 2012. Wide
1072 distribution and glacial origin of polar gypsum on Mars. Earth Planet. Sci. Lett. 317–
1073 318, 44–55.

1074 Mellon, M. T., Arvidson, R. E., Malin, M. C., Lemmon, M. T., Heet, T., Marshall, J., Sizemore,
1075 H. G., Searls, M. L., Phoenix Science Team, 2008. The Periglacial Landscape and
1076 Ground Ice at the Mars Phoenix Landing Site. AGU Fall Meeting Abstracts 14, 08.

1077 Milkovich, S. M., Head, J. W., 2005. North polar cap of Mars: Polar layered deposit
1078 characterization and identification of a fundamental climate signal. J. Geophys. Res.
1079 110 (E1), doi:10.1029/2004JE002349.

1080 Milkovich, S. M., Head, J. W., Gerhard, N., 2008. Stratigraphic analysis of the northern polar
1081 layered deposits of Mars: Implications for recent climate history. Planet. Space Sci.
1082 56 (2), 266-288.

1083 Montmessin, F., Harberle, R. M., Forget, F., Langevin, Y., Clancy R. T., Bibring, J.-P. On the
1084 origin of perennial water ice at the south pole of Mars: A precession-controlled
1085 mechanism? J. Geophys. Res. Planets. 112 (E8), doi:10.1029/2007JE002902.

1086 Moore, J.M., Mellon, M.T., Zent, A.P., 1996. Mass Wasting and Ground Collapse in Terrains
1087 of Volatile-Rich Deposits as a Solar System-Wide Geological Process: The Pre-
1088 Galileo View. Icarus 122, 63-78.

1089 Morgan, F., Seelos, F., Murchie, S., CRISM Team, 2009. 'CAT Tutorial', CRISM Data Users'
1090 Workshop at Lunar Planet. Sci. 40.

1091 Mouginot, J., Pommerol, A., Kofman, W., Beck, P., Schmitt, B., Herique, A., Grima, C.,
1092 Safaeinili, A., Plaut, J. J., 2010. The 3-5 MHz global reflectivity map of Mars by
1093 MARSIS/Mars Express: Implications for the current inventory of subsurface H_2O.
1094 Icarus 210 (2), 612-625.

1095 Newsom, H. E., Brittelle, G. E., Hibbitts, C. A., Crossey, L. J., Kudo, A. M., 1996. Impact
1096 crater lakes on Mars. J. Geophys. Res. 101 (E6), 14951-14955.

1097 Osinski, G. R., Lee, P., Parnell, J., Spray, J. G., Baron, M. T., 2005. A case study of impact-
1098 induced hydrothermal activity: The Haughton impact structure, Devon Island,
1099 Canadian high arctic. Meteorit. Planet. Sci. 40 (12), 1859-1877.

1100 Pankine, A. A., Tamppari, L. K., Smith, M. D., 2009. Water vapor variability in the north polar
1101 region of Mars from Viking MAWD and MGS TES datasets. Icarus 204 (1), 87-102.

1102 Perron, J. T., Mitrovica, J. X., Manga, M., Matsuyama, I., Richards, M. A., 2007. Evidence of
1103 an ancient martian ocean in the topography of deformed shorelines. Nature 447, 840-
1104 843.

1105 Perron, J. T., Huybers, P., 2009. Is there an orbital signal in the polar layered deposits on
1106 Mars? Geology 37 (2), 155-158.

1107 Phillips, R. J., Zuber, M. T., Smrekar, S. E., Mellon, M. T., Head, J. W., Tanaka, K. L.,
1108 Putzig, N. E., Milkovich, S. M., Campbell, B. A., Plaut, J. J., Safaeinili, A., Seu, R.,
1109 Biccari, D., Carter, L. M., Picardi, G., Orosei, R., Surdas Mohit, P., Heggy, E., Zurek,
1110 R. W., Egan, A. F., Giacomoni, E., Russo, F., Cutigni, M., Pettinelli, E., Holt, J. W.,
1111 Leuschen, C. J., Marinangeli, L., 2008. Mars north polar deposits: stratigraphy, age,
1112 and geodynamical response. Science 320 (5880), 1182-1185.

1113 Plaut, J. J., Safaeinili, A., Holt, J. W., Phillips, R. J., Head, J. W., Seu, R., Putzig, N. E.,
1114 Frigeri, A., 2009. Radar evidence for ice in lobate debris aprons in the mid-northern
1115 latitudes of Mars. Geophys. Res. Lett. 36, 02203.

1116 Putzig, N. E., Phillips, R. J., Campbell, B. A., Holt, J. W., Plaut, J. J., Carter, L. M., Egan, A.
1117 F., Bernardini, F., Safaeinili, A., Seu, R., 2009. Subsurface structure of Planum
1118 Boreum from Mars Reconnaissance Orbiter Shallow Radar soundings. Icarus 204
1119 (2), 443-457.

1120 Rathbun, J. A., Squyres, S. W., 2002. Hydrothermal Systems Associated with Martian
1121 Impact Craters. Icarus 157, 362-372.

1122 Rodríguez, J. A. P., Tanaka, K. L., Berman, D. C., Kargel, J. S., 2010. Late Hesperian plains
1123 formation and degradation in a low sedimentation zone of the northern lowlands of
1124 Mars. Icarus 210 (1), 116-134.

1125 Russell, P. S., Head, J. W., 2002. The martian hydrosphere/cryosphere system: Implications
1126 of the absence of hydrologic activity at Lyot crater. Geophys. Res. Lett. 29 (17),
1127 doi:10.1029/2002GL015178.

1128 Russell, P. S., Head, J. W., Hecht, M. H., 2003. Evolution of Volatile-rich Crater Interior
1129 Deposits on Mars. Sixth International Conference on Mars. Abstract 3256.

1130 Russell, P. S., J. W. Head, I., Hecht, M. H., 2004. Evolution of Ice Deposits in the Local
1131 Environment of Martian Circum-Polar Craters and Implications for Polar Cap History.
1132 Lunar Planet. Sci. 35. Abstract 2007.

1133 Russo, F., Cutigni, M., Orosei, R., Taddei, C., Seu, R., Biccari, D., Giacomoni, E., Fuga, O.,
1134 Flamini, E., 2008. An incoherent simulator for the SHARAD experiment. Radar
1135 Conference, RADAR '08. IEEE, Rome, Italy, doi:10.1109/RADAR.2008.4720761

1136 Sakimoto, S. E. H., 2005. Central Mounds in Martian Impact Craters: Assessment as
1137 Possible Perennial Permafrost Mounds (Pingos). Lunar Planet. Sci. 36. Abstract
1138 2099.

1139 Seelos, K. D., Seelos, F. P., Titus, T. N., Murchie, S. L., Crism, T., 2008. CRISM
1140 Observations of Persistent Water Ice Deposits in the Northern Plains of Mars. Lunar
1141 Planet. Sci. 39. Abstract1885.

1142 Selvans, M. M., Plaut, J. J., Aharonson, O., Safaeinili, A., 2010. Internal structure of Planum
1143 Boreum, from Mars advanced radar for subsurface and ionospheric sounding data. J.
1144 Geophys. Res. 115 (E9), doi:10.1029/2009JE003537.

1145 Smith, D. E., Zuber, M. T., Neumann, G. A., 2001. Seasonal Variations of Snow Depth on
1146 Mars. Science 294 (5549), 2141-2146.

1147 Smith, I. B., Holt, J. W., 2010. Onset and migration of spiral troughs on Mars revealed by
1148 orbital radar. Nature 465 (7297), 450-453.

1149 Spiga, A., Forget, F., Madeleine, J.-B., Montabone, L., Lewis, S.R., Millour, E., 2011. The
1150 impact of martian mesoscale winds on surface temperature and on the determination
1151 of thermal inertia. Icarus 212, 504–519.

1152 Stepinski, T. F., Mendenhall, M. P., Bue, B. D., 2009. Machine cataloging of impact craters
1153 on Mars. Icarus 203 (1), 77-87.

1154 Tanaka, K. L., Skinner Jr, J. A., Hare, T. M., 2005. Geologic map of the northern plains of
1155 Mars. Scientific Investigation Map 2888. USGS/NASA.

1156 Tanaka, K. L., Hayward, R. K., 2008. Mars' North Circum-Polar Dunes: Distribution,
1157 Sources, and Migration History. Planetary Dunes Workshop: A Record of Climate
1158 Change, held April 29-May 2, 2008 in Alamogordo, New Mexico. Abstract1403, p.69-
1159 70.

1160 Tanaka, K. L., Rodriguez, J. A. P., Skinner Jr, J. A., Bourke, M. C., Fortezzo, C. M.,
1161 Herkenhoff, K. E., Kolb, E. J., Okubo, C. H., 2008. North polar region of Mars:
1162 Advances in stratigraphy, structure, and erosional modification. Icarus 196 (2), 318-
1163 358.

1164 Titus, T.N., Kieffer, H.H., Mullins, K.F., Christensen, P.R., 2001. TES premapping data: Slab
1165 ice and snow flurries in the Martian north polar night. J. Geophys. Res. 106, 23181-
1166 23196, doi : 10.1029/2000JE001284.

1167 Vincendon, M., 2008. Modélisation du transfert radiatif dans l’atmosphère martienne pour la
1168 détermination des propriétés spectrales de surface et la caractérisation des aérosols

1169 martiens à partir des données OMEGA. PhD Thesis, Université de Paris-Sud XI, pp.
1170 193.

1171 Vincendon, M., Langevin, Y., Poulet, F., Bibring, J. P., Gondet, B., Schmitt, B., Douté, S.,
1172 2006. Surface Water Ice and Aerosols Evolution of 77°N, 90°E Mars Crater During
1173 Early Summer by OMEGA/MEx. Lunar Planet. Sci. 37. Abstract 1769.

1174 Vincendon, M., Forget, F., Mustard, J., 2010. Water ice at low to midlatitudes on Mars. J.
1175 Geophys. Res. 115, doi:10.1029/2010JE003584.

1176 Wagstaff, K. L., Titus, T. N., Ivanov, A. B., Castaño, R., Bandfield, J. L., 2008. Observations
1177 of the north polar water ice annulus on Mars using THEMIS and TES. Planet. Space
1178 Sci. 56 (2), 256-265.

1179 Westbrook, O.W., 2009. Crater ice deposits near the south pole of Mars. Masters Thesis,
1180 Massachusetts Institute of Technology, pp. 60.

1181

Figure Captions

Figure 1: Depth-diameter plot of all the craters north of 65°N, with ice-filled craters and dune-filled craters highlighted. Lines extending above the mound-points are the predicted depths of the craters with the mounds removed. Depth-diameter relationship derived for polar craters by Garvin et al. (2000) and the general relationship for Martian craters (Garvin, 2005) are marked. An anomalous pixel in the MOLA data has resulted in a ~1.5 km crater with >1 km depth, we believe this pixel to be an error in the data; hence this point should be ignored.

Figure 2: Map of the north polar region of Mars made from MOLA topography with overlain hillshade. It includes the locations of the mounds studied and locations of the swaths used to produce Fig. 4. Outlined in grey are all the craters included in the survey. The "+" indicates the position of crater 332, which is mentioned in the text, but does not have a significant mound. "OM" indicates the position of Fig. 17, with the arrow showing the viewing direction. "Complete dune cover" means that the mound spans the whole crater floor and is covered in dunes and "dune-covered mounds" are those which are covered in dunes, but only occupy part of the crater floor (the rest of the crater floor is dune-free.)

Figure 3: Left, Crater 388 Dokka. Perspective view (with 3x vertical exaggeration) of a subset of HRSC nadir (RGB-color online) image H1177_0000 draped over MOLA topography with profiles A-A' and B-B' marked and shown beneath. Right: Crater 811. Perspective view (with 3x vertical exaggeration) of a subset of HRSC nadir (RGB-color online) image H3711_0000 draped over MOLA topography with profiles C-C' and D-D' marked. The 20 m scale vertical roughness on profiles C and D is a result of the overlying dunes. Arrow points to North in both figures. Profiles A, B, C and D were generated from

1207 MOLA topography – note the exaggeration of the vertical scale. Credit for HRSC images
1208 ESA/DLR/FU Berlin (G. Neukum).
1209
1210 Figure 4: Histogram plots of the elevation variation with latitude within the swaths outlined in
1211 Fig. 2. Black (blue online) indicates craters with ice-mounds and the height to which those
1212 mounds reach, labels correspond to those in Fig. 2 and Table 1. Note that the vertical scale
1213 is exaggerated.
1214
1215 Figure 5: Bar chart of calculated mound volume for each crater in descending order. Note
1216 the logarithmic scale on the y-axis. The mean value (314.7 km^3) is indicated by the upper
1217 dashed line and the median value (17.01 km^3) by the lower dotted line.
1218
1219 Figure 6: Right optical image with scale and north arrow, and left optical image overlain by
1220 proportion of water ice detected (band depth at 1.5 μm).
1221 (A) Korolev crater (206), optical images from MRO CTX P20_008831_2529_XN_72N195W
1222 (L_s 85.33°), P21_009042_2528_XI_72N197W (L_s 92.58°),
1223 P21_009332_2529_XN_72N194W (L_s 102.66°), P22_009477_2530_XN_73N193W (L_s
1224 107.77°), P22_009754_2529_XN_72N195W (L_s 117.69°), and OMEGA track 0987_2 (L_s
1225 105.9°).
1226 (B) Dokka crater (388), optical images MRO CTX B01_010108_2573_XN_77N144W (L_s
1227 130.74°) and B02_010385_2572_XN_77N146W (L_s 141.32°), OMEGA track 1221_1 (L_s
1228 136.4°).
1229 (C) Crater 544, optical images THEMIS V13697003 (L_s 144.508) and V12474005 (L_s
1230 97.106°), OMEGA track 1257_0 (L_s 141.3°).
1231 (D) Crater 579, optical image MRO CTX P02_001819_2570_XN_77N270W (L_s 151.16°),
1232 OMEGA track 1017_1 (L_s 109.5°).

(E) Louth crater (503), optical image HRSC h1343_0001 (L_s 153.5°), OMEGA track 1017_1 (L_s 109.5°). Credit for CTX images NASA/JPL/MSSS, for HiRISE images NASA/JPL/University of Arizona, for THEMIS images NASA/JPL/ASU, for HRSC images ESA/DLR/FU Berlin (G. Neukum), for OMEGA data ESA/OMEGA.

Figure 7: Maps of layer exposures and measured layer dips in Korolev (206), Dokka (338), crater 579, Louth (503), crater 769 and crater 663. Shaded areas represent areas where layers were observed to be cropping out, dotted lines are selected layers to illustrate the nature of the layering and the dip and strike labels are in units of degrees. Dotted box in panel 579 indicates the approximate location of Fig. 10. Images all MRO CTX: **206 Korolev**: P20_008831_2529_XN_72N195W, P21_009042_2528_XI_72N197W, P21_009332_2529_XN_72N194W, P22_009477_2530_XN_73N193W, P22_009754_2529_XN_72N195W, **388 Dokka**: B01_010108_2573_XN_77N144W and B01_010108_2573_XN_77N144W, **579**: P02_001819_2570_XN_77N270W, **503 Louth**: P01_001370_2503_XI_70N257W, **769**: B02_010407_2587_XN_78N028W, **663**: P20_008795_2592_XN_79N299W. Image credit NASA/JPL/MSSS.

Figure 8: Boxplots of the estimated layer spacing in mounds and polar deposits. The vertical bars are the median values, the boxes delimit the interquartile range, the whiskers the range and the dots are the outliers (data points outside 1.5 interquartile ranges from the box). In grey are measurements made outside craters. Shorthand labels are as follows: **206 Korolev** – layers measured in Korolev crater in CTX images P20_008831_2529_XN_72N195W and P21_009042_2528_XI_72N197W**, 388 Dokka** – layers measured in Dokka crater in CTX images B01_010108_2573_XN_77N144W and B02_010385_2572_XN_77N146W**, 503 Louth HR** - layers proximal to dunes in Louth crater measured in HiRISE PSP_001700_2505, **503 Louth CTX** – layers measured in CTX image P01_001370_2503_XI_70N257W at the edge of the mound in Louth, **579**: layers identified in

crater 579 in HiRISE image PSP_008926_2575, **663** - layers measured in crater 663 corrected for layer dip as well as exposure slope, in HiRISE image ESP_016087_2595, **769** – layers measured in crater 769 in HiRISE image PSP_008416_2585, **PLD1** – layers measured in the PLD in HiRISE image PSP_010366_2590, PLD2 - layers measured in the polar layer deposits in HiRISE image TRA_000825_2665 and **PLD3** - layers measured in the polar layer deposits in HiRISE image TRA_000863_2640, upper quartile is at 15.0 m and the upper whisker at 29.3 m, with one outlier at 39.8 m. **BU** – layers measured in the polar basal deposits in HiRISE image TRA_000863_2640.

Figure 9: Histogram of mound slopes on layer exposure sites (as shown in Fig.7) as derived from 128 pixel/degree MOLA data. The mean of the distribution is 4.4° with a standard deviation of 3.6° and skew of 1.29.

Figure 10: Detailed sketch (left) cross section (top right) and detail-inset (bottom-right) of the layer stratigraphy in crater 579. On the sketch dotted lines are selected layers to illustrate the nature of the layering, bold lines are the locations of unconformities and dip and strike symbol labels are in units of degrees. The line labeled I-II indicates the position of the cross section adjacent to the image. Colored lines are contours in 25 m intervals derived from gridded MOLA 128 pixel/degree data (see online for color version). The crater wall is located to the right in both the sketch and the cross-section. Overlain on the sketch is the CTX image P02_001819_2570_XN_77N270W, credit NASA/JPL/MSSS. Labels A, B and C are packets of layers separated by unconformities. On the cross-section dotted lines show the estimated position of the unconformities and the relative vertical positions of the three layer packets A, B and C. From layer cross-cutting relationships we know that A is older than B, which is older than C; hence the packets were laid down in an upwards younging sequence. The location of the inset is indicated by the grey box. The image in the inset is HiRISE image PSP_008926_2575; credit NASA/JPL/University of Arizona.

Figure 11: Depth-corrected SHARAD radargram r_0554201_001 and clutter simulation for Korolev (206) crater. South is to the right.

Figure 12: Map of the mound center-of-mass offsets with respect to the crater center (normalized by crater diameter) with the mapped location of north pole dunefields and wind vectors from dune slipface measurements taken from Tanaka and Hayward (2008). The vector linking the center of mass of the ice mound to the centroid of the crater rim polygon we use as a representation of the asymmetry of the mounds. Dune density is given as the relative density parameter calculated by Tanaka and Hayward (2008) as the ratio of mean dune length vs. dune crest separation.

Figure 13: The variation of bolometric brightness temperature with season (L_s), inside and on the ice-free plains outside two example craters as derived from TES data downloaded using the TES Data Tool – http://tes.asu.edu/data_tool/ for Mars years 24 to 28. The dataset contains both data collected at 2pm and 2am local solar time; hence there are two distinct temperatures between 90-180° L_s when the sun is above the horizon at 2pm. Dokka Crater (388), a 51 km diameter crater which contains a dome of water ice, which suppresses the temperature almost all year round relative to that outside the crater. Crater 1065, at 70°N, 352°E diameter ~ 40 km, which has lower temperatures than the exterior only between L_s 250° and L_s 320°. The grey band indicates the water frost point temperatures corresponding to an atmospheric water content of between 10 and 60 prμm (Pankine et al., 2009).

Figure 14: Location of temporary ice deposits which remain after the seasonal cap has retreated, as indicated by arrows. The background is a MOLA hillshade image. A: Deposits around crater 561 at 267°E, 70°N form a plume extending to the east, matching dominant wind directions in this area (Fig. 12). CTX images P17_007799_2513_XN_71N093W and

P18_007944_2506_XN_70N092W. B: Deposits around crater 263 at 146°E, 72°N are located mainly on north-facing slopes, CTX image B01_009847_2522_XN_72N214W. Image credit MSSS/NASA/JPL.

Figure 15: Schematic diagram of the initiation and growth of ice domes, with the ices throughout as labeled in the first panel. North is to the right in all diagrams. The thickness of the frost and ice deposits are greatly exaggerated for illustration purposes. 1. In winter the microclimate in the crater provokes additional deposition of CO_2 and water ice inside the crater. 2. During the springtime sublimation, the CO_2 layer inside the crater remains (because a thicker layer takes longer to sublime), while the crater exterior is denuded of CO_2 and the H_2O starts to sublime. The H_2O released from the plains around the crater can be re-deposited in the crater interior, because of its lower temperature (as the CO_2 remains).3. Once the CO_2 has completely sublimed, relatively thick deposits of H_2O remain in the crater (H_2O from winter plus the H_2O re-condensed onto the CO_2), which act as a cold trap for H_2O subliming outside the crater. In addition the higher atmospheric pressure inside the crater reduces the rate of sublimation of this water ice. 4. The additional thickness and the reduced sublimation enable the survival of at least several meters thick deposit of water ice through the summer, which then builds up each year. A perennial deposit creates a positive feedback whereby higher thermal inertia and higher albedo than the surrounding landscape promotes continued deposition of water ice.

Figure 16: Perspective view of polar outliers near Olympia Mensae at 96.5°E, 74°N. Vertical exaggeration is five times. Outcrop in foreground is ~350 m tall and 10 km wide at the base. CTX images P21_009295_2550_XN_75N263W and P20_009018_2543_XI_74N262W used for topographic drape. Background hillshade and topography from the MOLA gridded 256 tile. CTX image credit MSSS/NASA/JPL.

Supp. Mat. Figure Captions

Figure S1: MOLA hillshade image and cross sections for all 18 craters with mounds. The black line on the image corresponds to the black north-south cross section on the plot, where “N” on the image indicates the northern end. The red line indicates the position of red east-west cross section on the plot (always oriented E-W apart from for crater 503, Louth). Data from the 256 pix/deg MOLA gridded data were used to produce the hillshade and cross sections for craters 206, 503, 579, 811, 814, 882, 904 and 934; for the others the data are derived from the 512 pix/deg gridded data.

1349 Table 1: Summary of the characteristics of the mounds and their host craters.[a]

Crater ID	Depth (m)	Diameter (km)	Longitude (°E)	Latitude (°N)	Distance to cap (km)	SwathID	Predicted depth (m)	Max. mound thickness (m)	Mound volume (km^3)	Garvin¤ ID	Garvin¤ mound volume (km^3)	Garvin¤ predicted initial depth (m)	Presence of Dunes	Mound planimetric area		Mound relief		Max. slope (°)	Mean slope (°)	Mound summit to rim distance (m)	
														absolute (km^2)	as % of crater area	absolute (m)	as % of depth			absolute	as % of depth
206 Korolev	3102	82.83	164.49	72.75	624	5	3133	1845	3848.5	E	1356	2860	none	3134	56	1818	59	33.5	3.5	1284	41
332[#]	1364	21.35	195.59	76.97	330	5	n/c	n/c	n/c	G	2.5	660	partial	n/c	n/c	117*	9*	n/c	n/c	1039*	76*
388 Dokka	2508	51.26	214.29	77.17	301	6	3053	1890	1318.9	D	463	1540	none	1115	53	1443	58	28.7	4.0	1065	42
436	1248	19.66	190.08	81.59	60	5	2069	1640	95.9	A	59	640	partial	129	43	909	73	23.1	6.2	339	27
480	936	16.13	240.14	78.11	119	6	930	383	4.4				100%	30	14	407	44	22.7	5.7	529	56
503 Louth	1788	36.15	103.24	70.17	568	4	1766	267	13.3				partial	136	12	400	22	14.5	3.2	1388	78
515	250	11.21	117.25	81.36	0	4	305	139	2.4				none	37	37	118	47	3.8	1.1	133	53
544	773	20.96	255.07	81.27	0	6	788	378	21.0	F	35	610	none	107	42	686	89	10.4	3.7	87	11
577	248	11.73	88.93	81.16	0	4	284	133	2.4				none	32	52	157	63	4.5	1.4	72	31
579	1173	30.53	89.13	77.11	130	4	1517	932	201.6	B	248	1170	none	485	65	736	63	19.4	2.5	437	37
663	1451	24.60	60.92	79.13	0	3	1836	1017	59.1	H	3.4	600	partial	126	28	822	57	23.7	4.3	629	43
697	151	9.52	47.62	79.76	0	3	161	94	1.0				none	21	46	103	68	3.8	1.6	13	11
769	1058	20.19	331.72	78.59	8	1	1103	512	21.1	C	34	680	partial	96	29	685	65	15.1	4.9	374	35
795	371	12.55	347.00	78.61	0	1	371	178	3.1				none	41	32	274	74	6.8	2.5	98	26
811	571	18.82	309.02	71.20	452	2	773	565	40.4				100%	138	49	380	67	17.2	3.3	191	33
814	694	16.95	319.18	74.25	257	2	666	408	20.7				100%	97	41	457	66	19.8	4.1	237	34
882	572	16.32	340.23	75.05	190	1	543	150	1.8				100%	29	13	192	33	9.2	2.5	381	67
904	993	22.59	346.90	74.63	186	1	942	121	0.8				100%	84	20	178	18	20.1	2.9	488	73
934	666	15.86	348.27	73.54	249	1	653	240	7.2				100%	28	14	368	55	9.8	2.2	626	63

Min.	151	9.52	70.17	0	161	94	0.8	21	12	103	9	3.8	1.1	13	11
Mean	1048	24.33	76.97	183	1161	605	314.7	326	36	563	54	15.9	3.3	495	44
Median	936	19.24	77.17	130	859	381	17.0	96	39	403	59	16.2	3.2	381	41
Max.	3102	82.83	81.59	624	3133	1890	3848.5	3134	65	1818	89	33.5	6.2	1388	78

[a] Abbreviations and symbols used: Max. = maximum, Min. = minimum, Garvin¤ refers to results in Garvin et al. (2000), # refers to the crater that has layered deposits, but no significant mound, n/c = not calculated, and * indicates that the relief was estimated from a MOLA cross profile, rather than taking the difference between the max. and min. MOLA elevations found within the mound polygon.

Highlights:

- 18 potentially ice-cored mounds were found in craters in Mars' north polar region.
- The stratigraphy of the mounds argues for deposition from the atmosphere.
- We argue many of them were deposited separately from the polar cap.
- The crater micro-environment is a potential explanation for mound initiation.
- These mounds are sensitive and important records of Amazonian climate on Mars.

Figure1 (black and white)

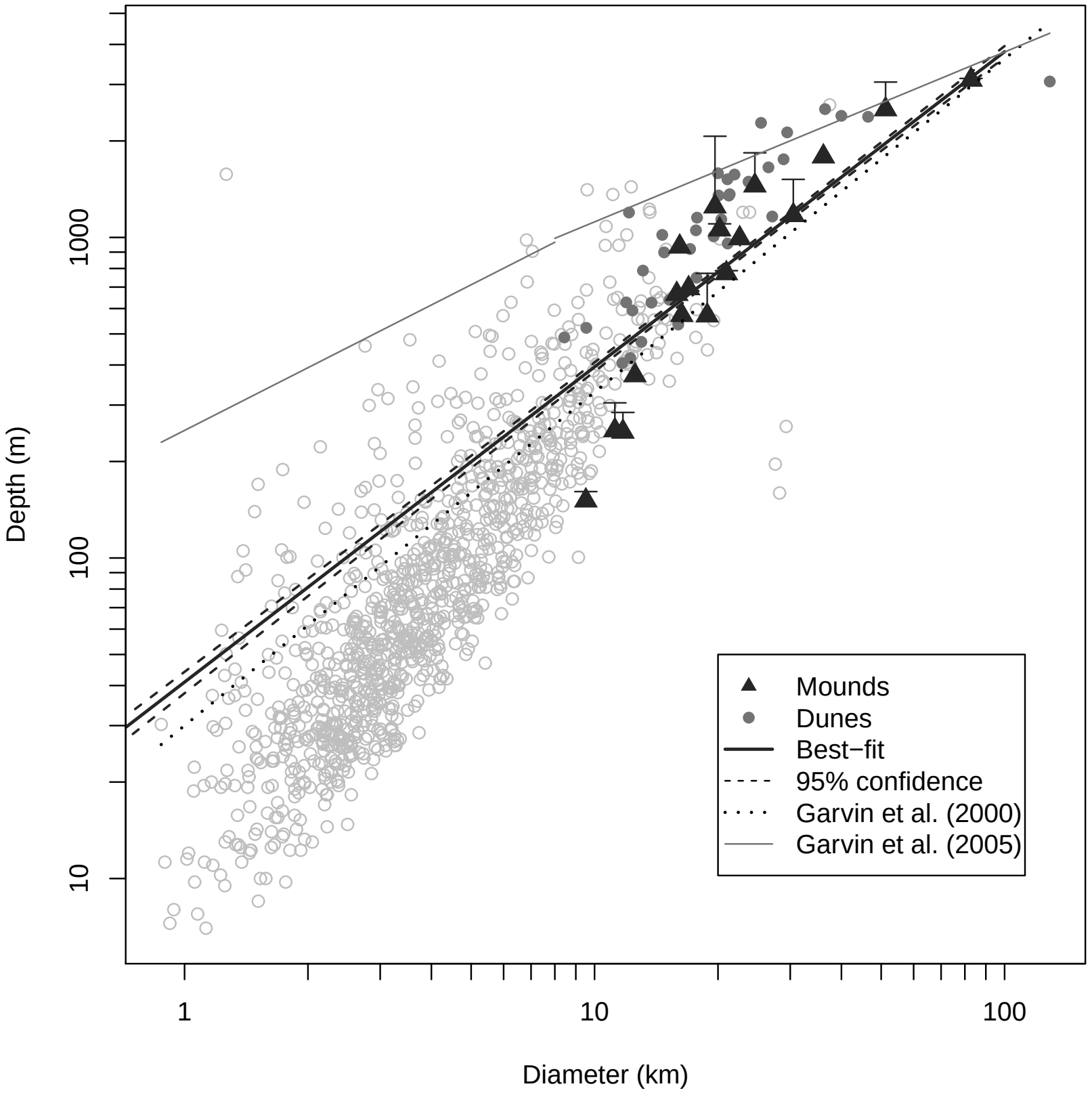

Figure1

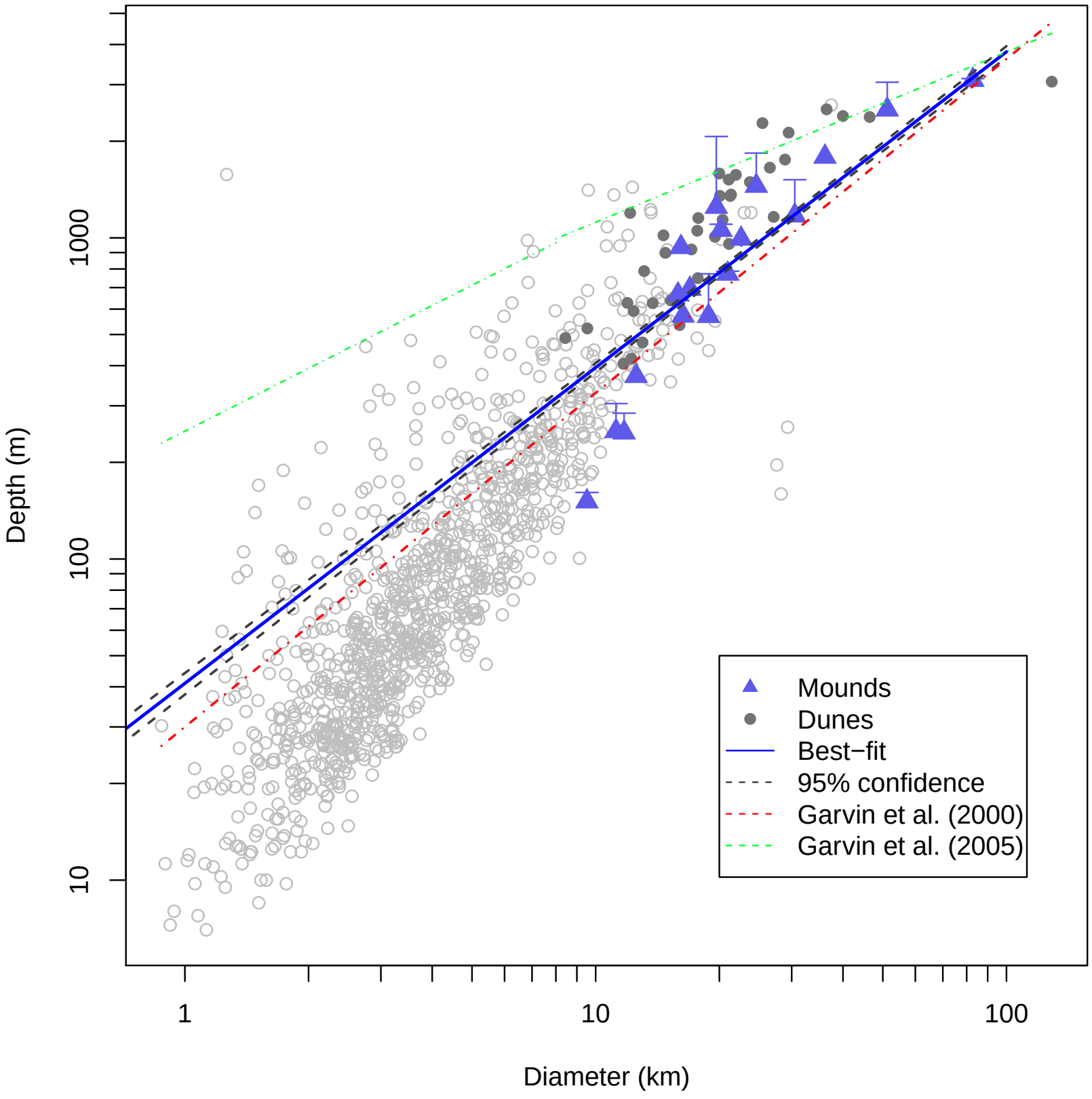
Depth (m)
10
100
1000
1
10
100
Diameter (km)
Mounds
Dunes
Best−fit
95% confidence
Garvin et al. (2000)
Garvin et al. (2005)

Figure 2 (black and white)
Click here to download high resolution image

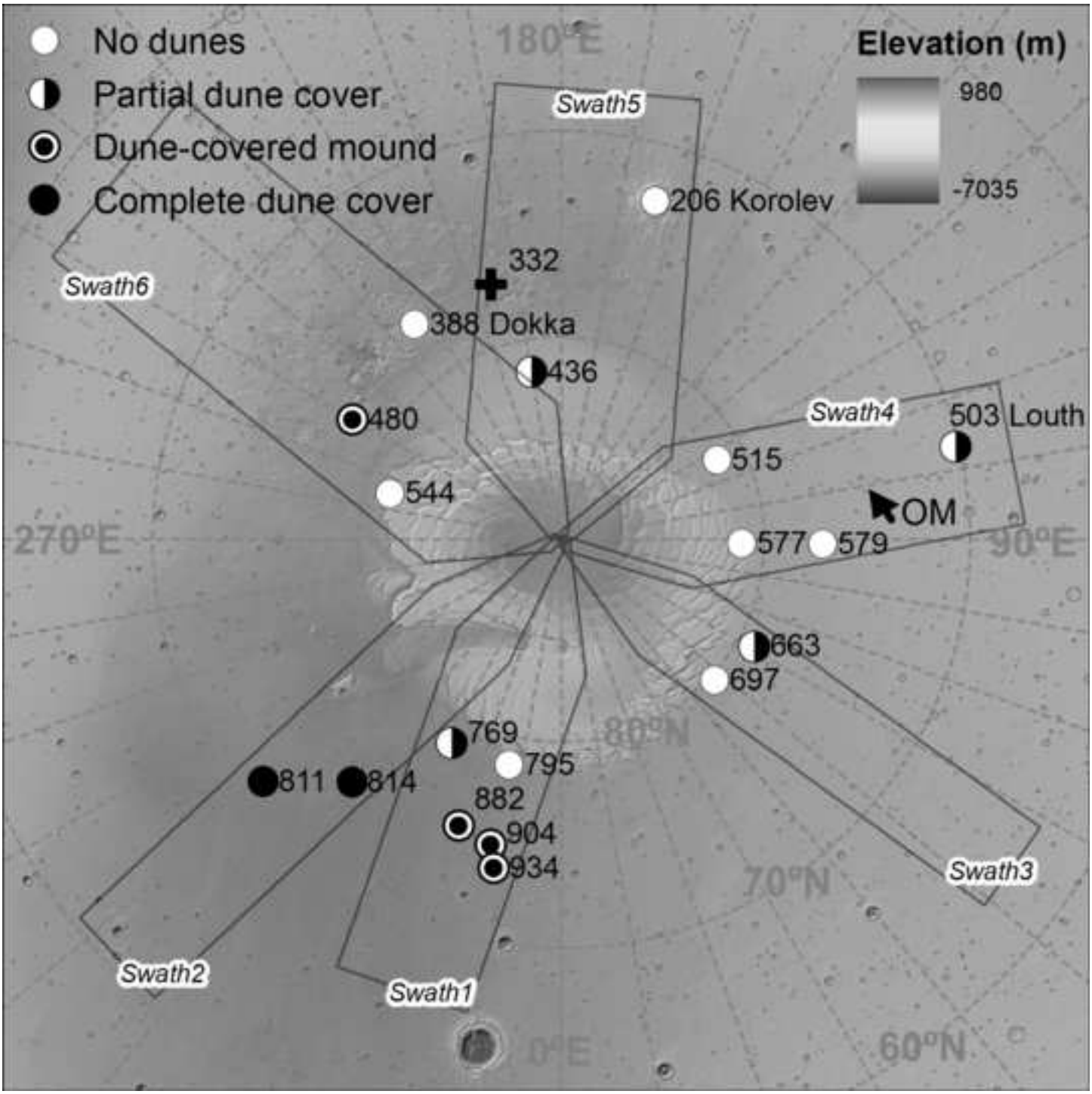

Figure 2

Click here to download high resolution image

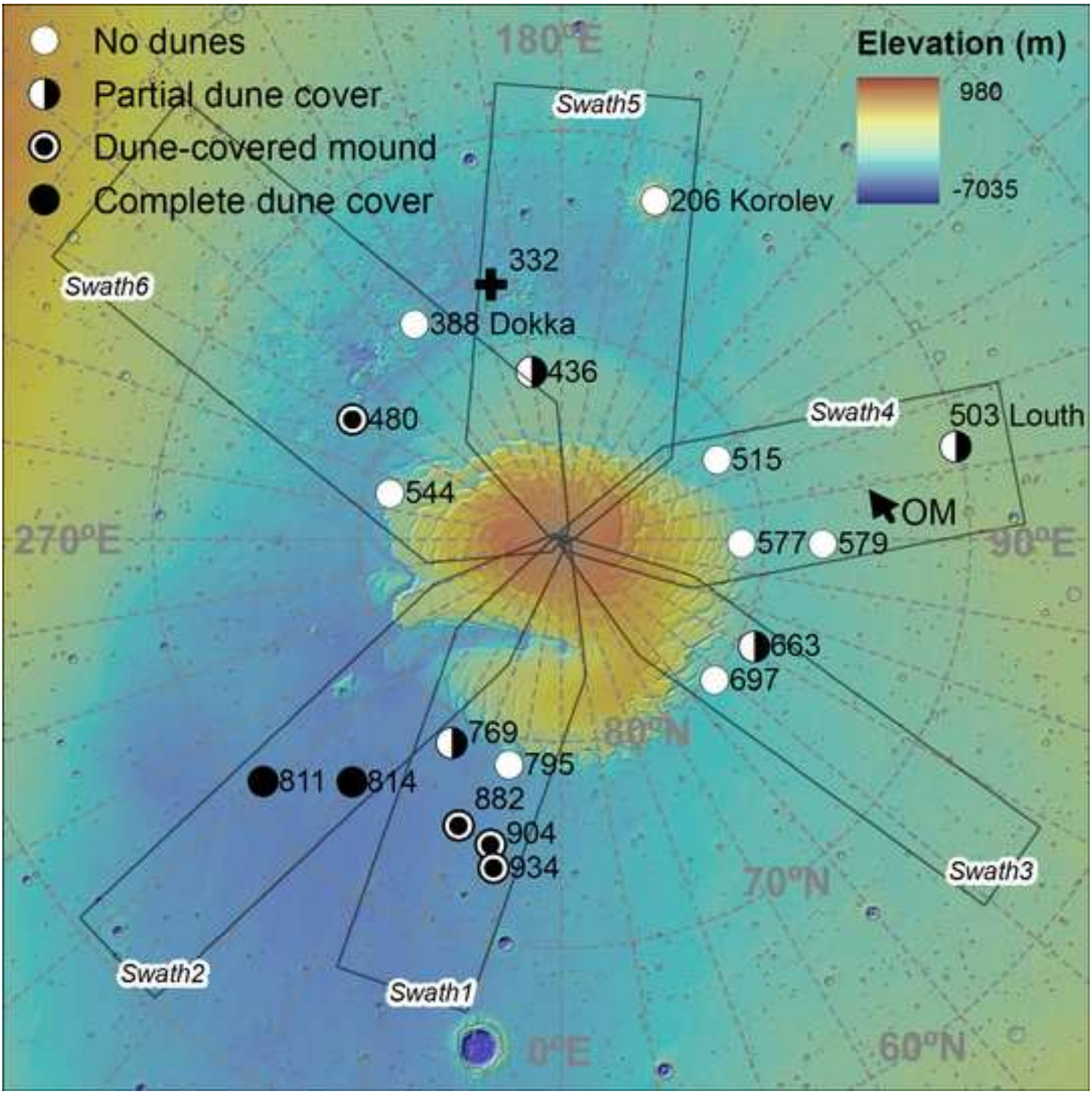

Figure 3 (black and white)
Click here to download high resolution image

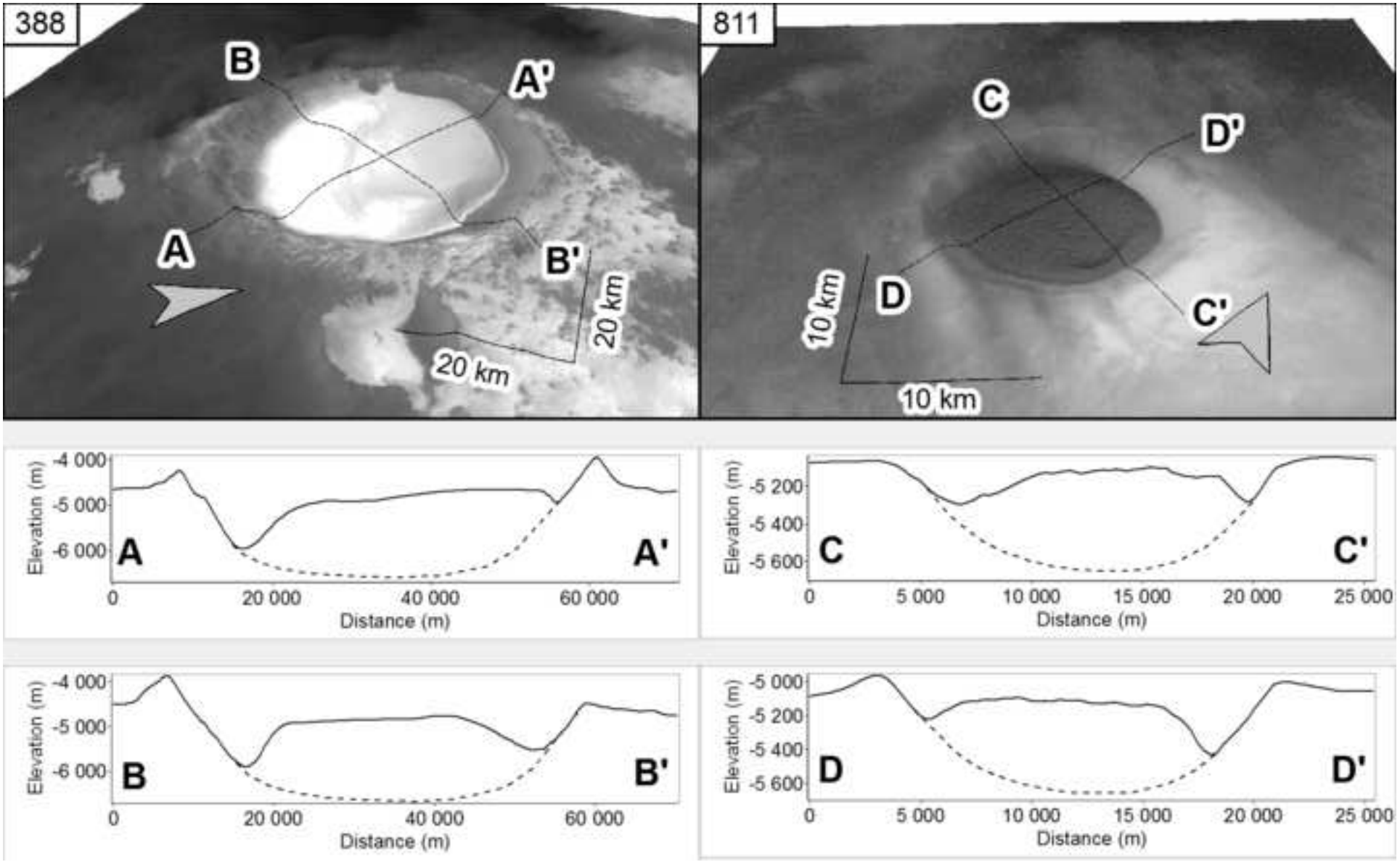

Figure 3

Click here to download high resolution image

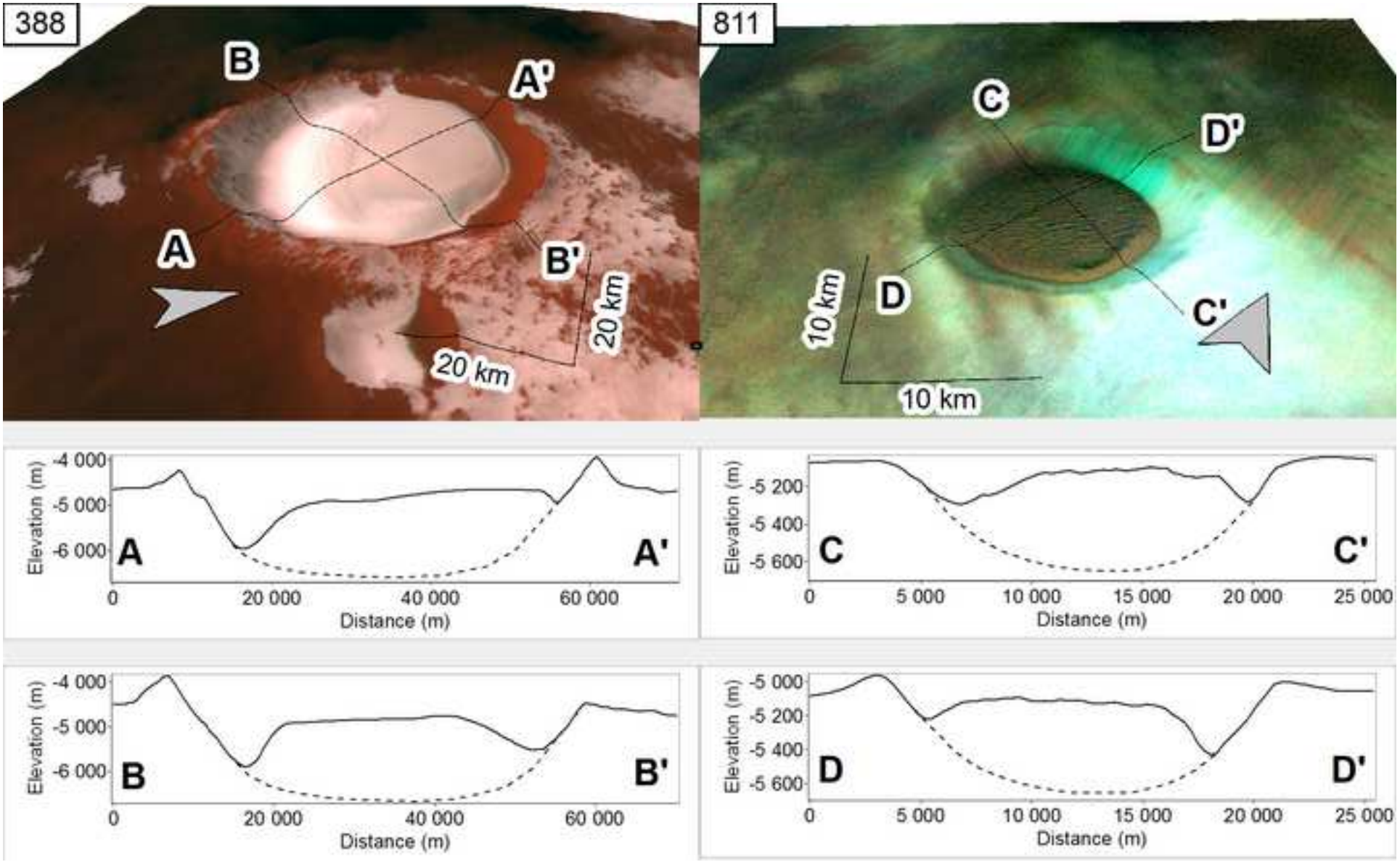

Figure 4 (black and white)

Click here to download high resolution image

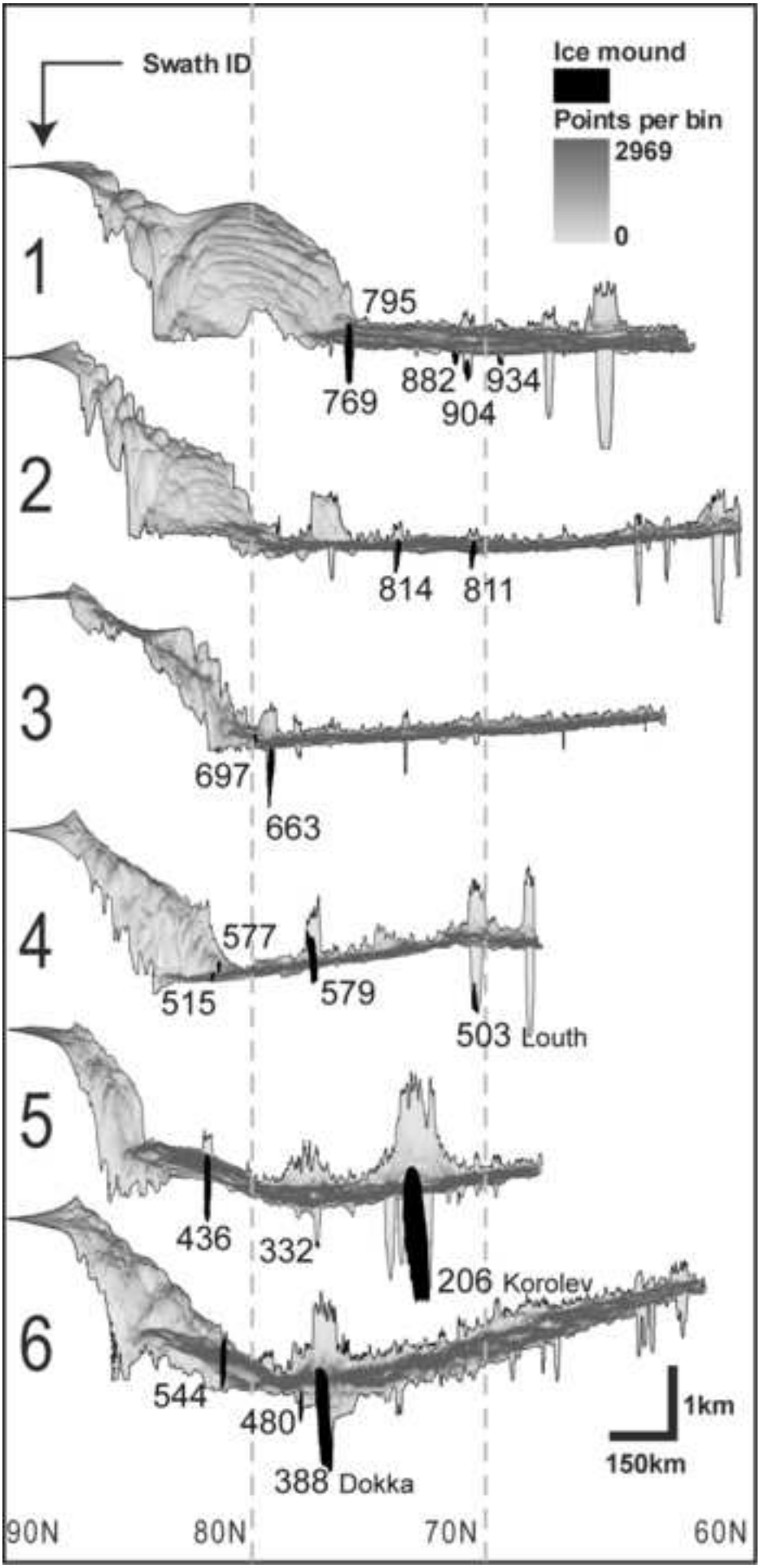

Figure 4

Click here to download high resolution image

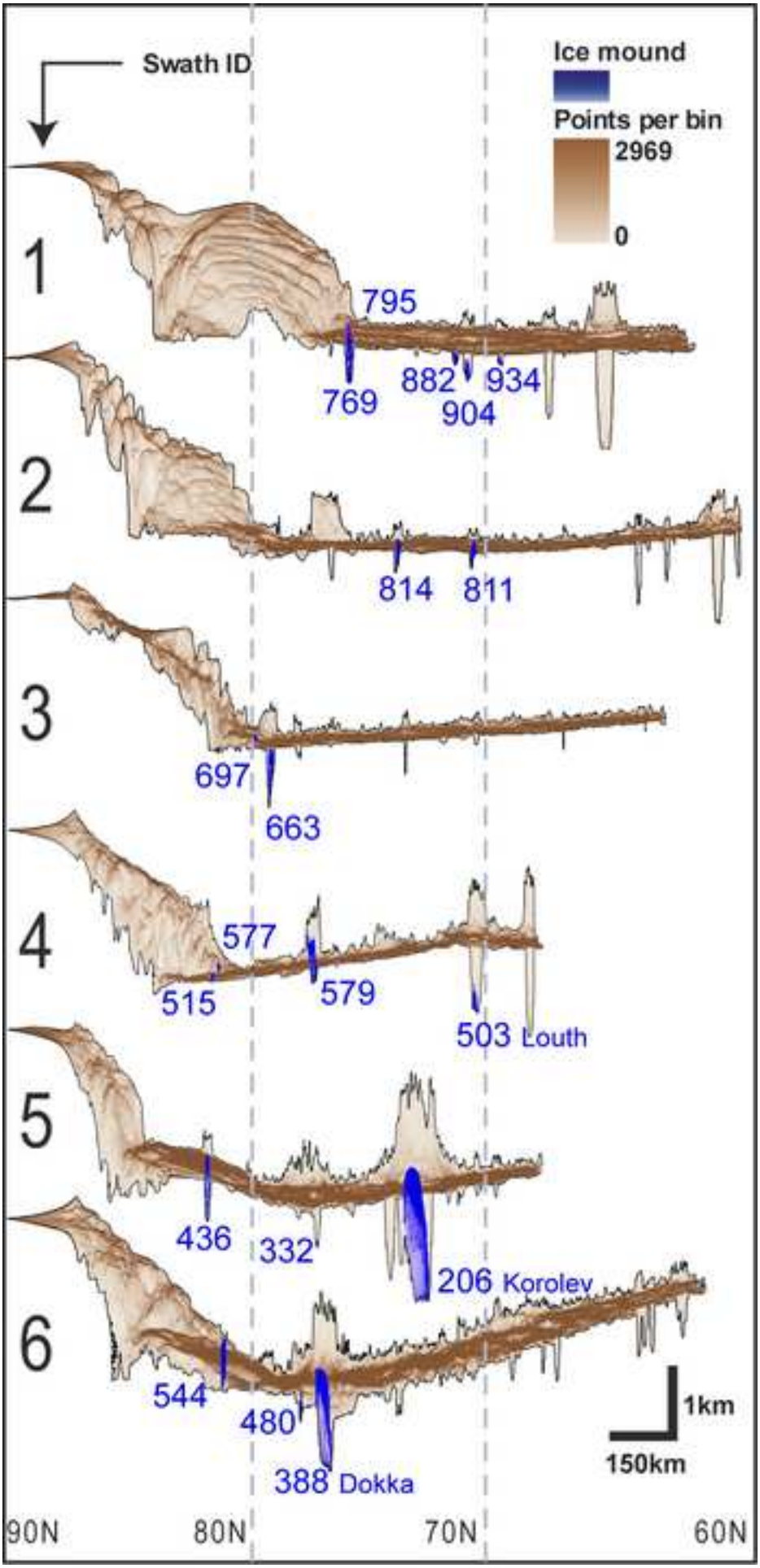

Figure 5 (black and white)

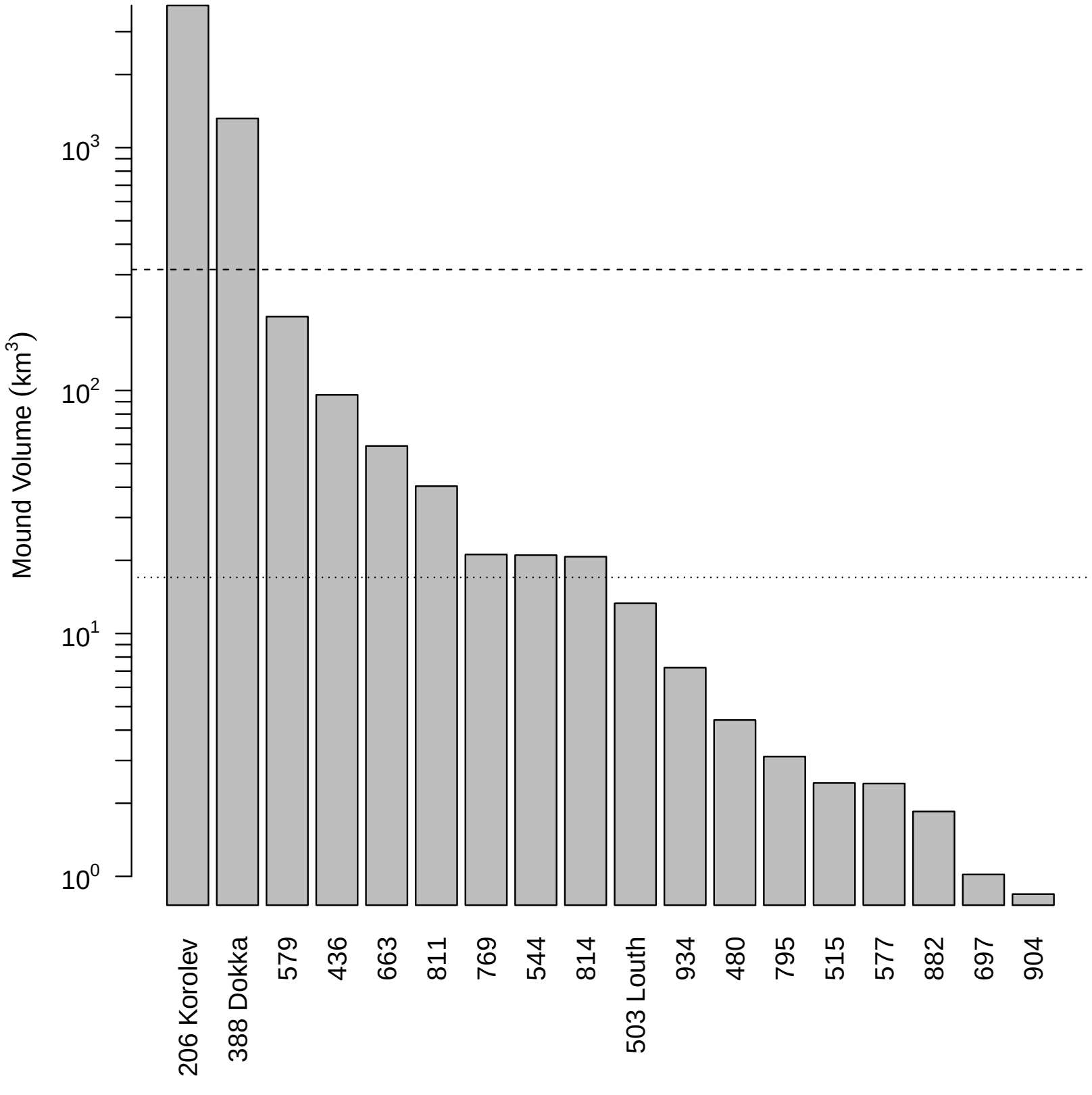

Figure 6 (black and white)
Click here to download high resolution image

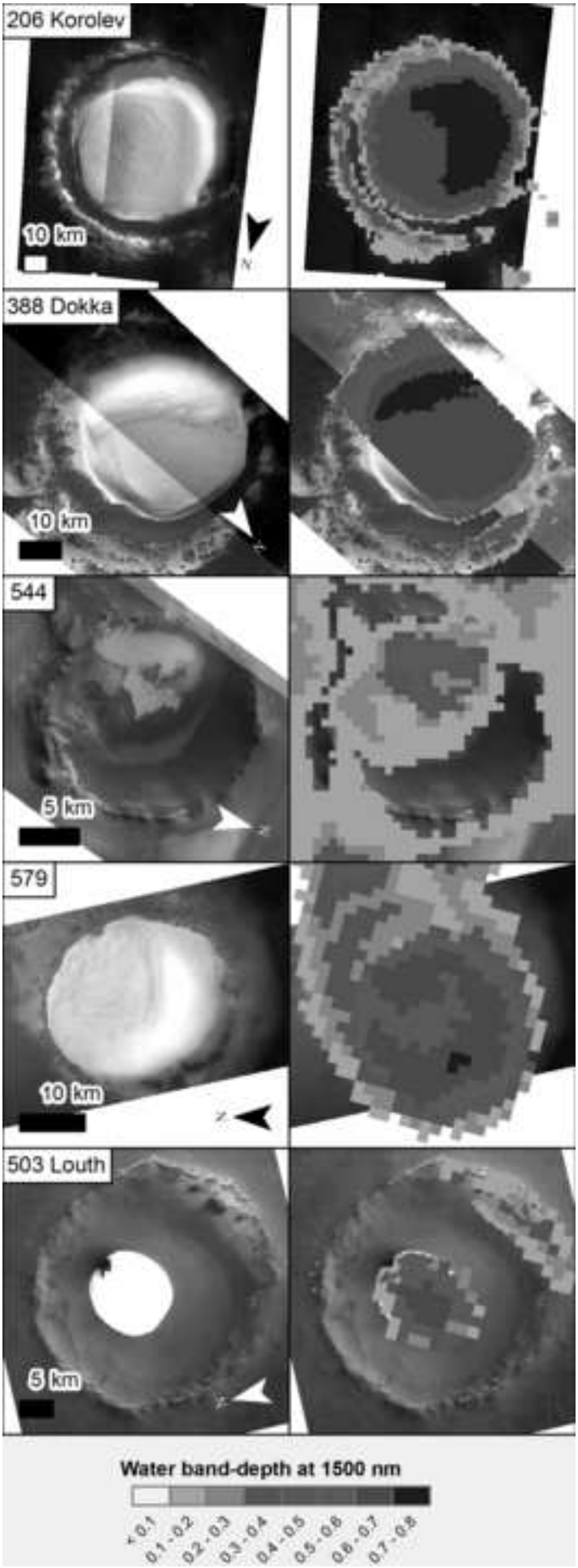

Figure 6

Click here to download high resolution image

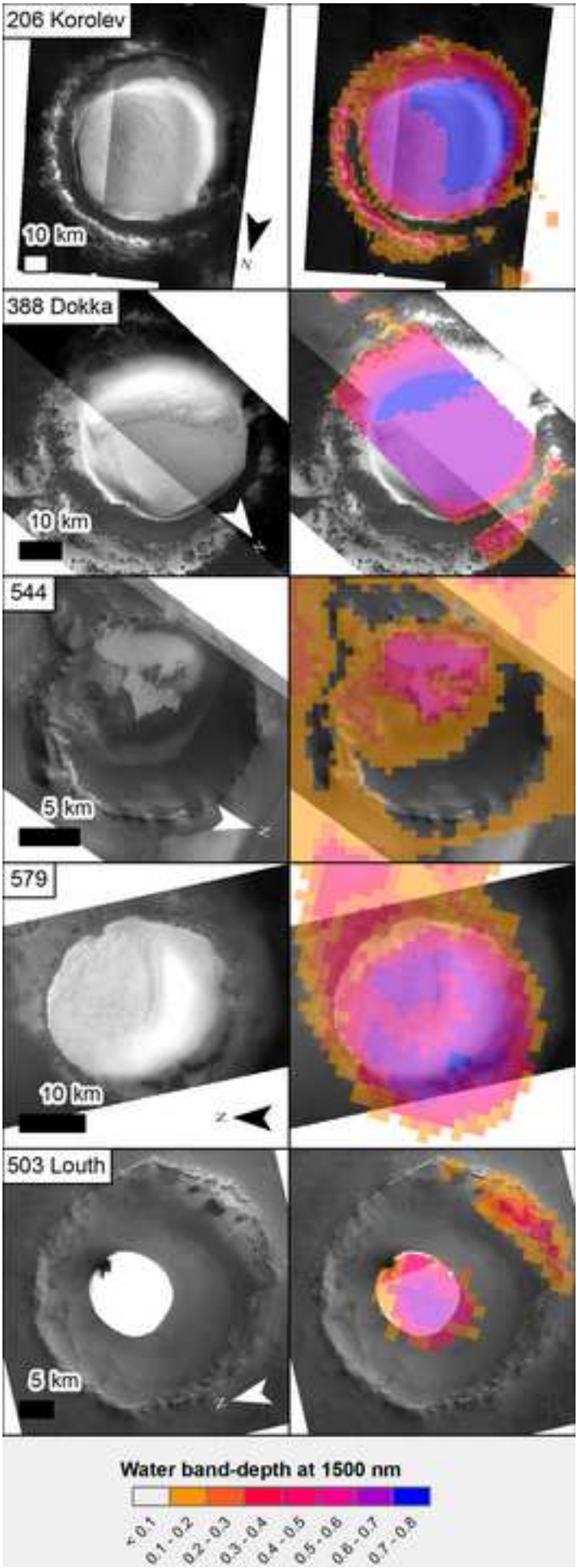

Figure 7 (black and white)
Click here to download high resolution image

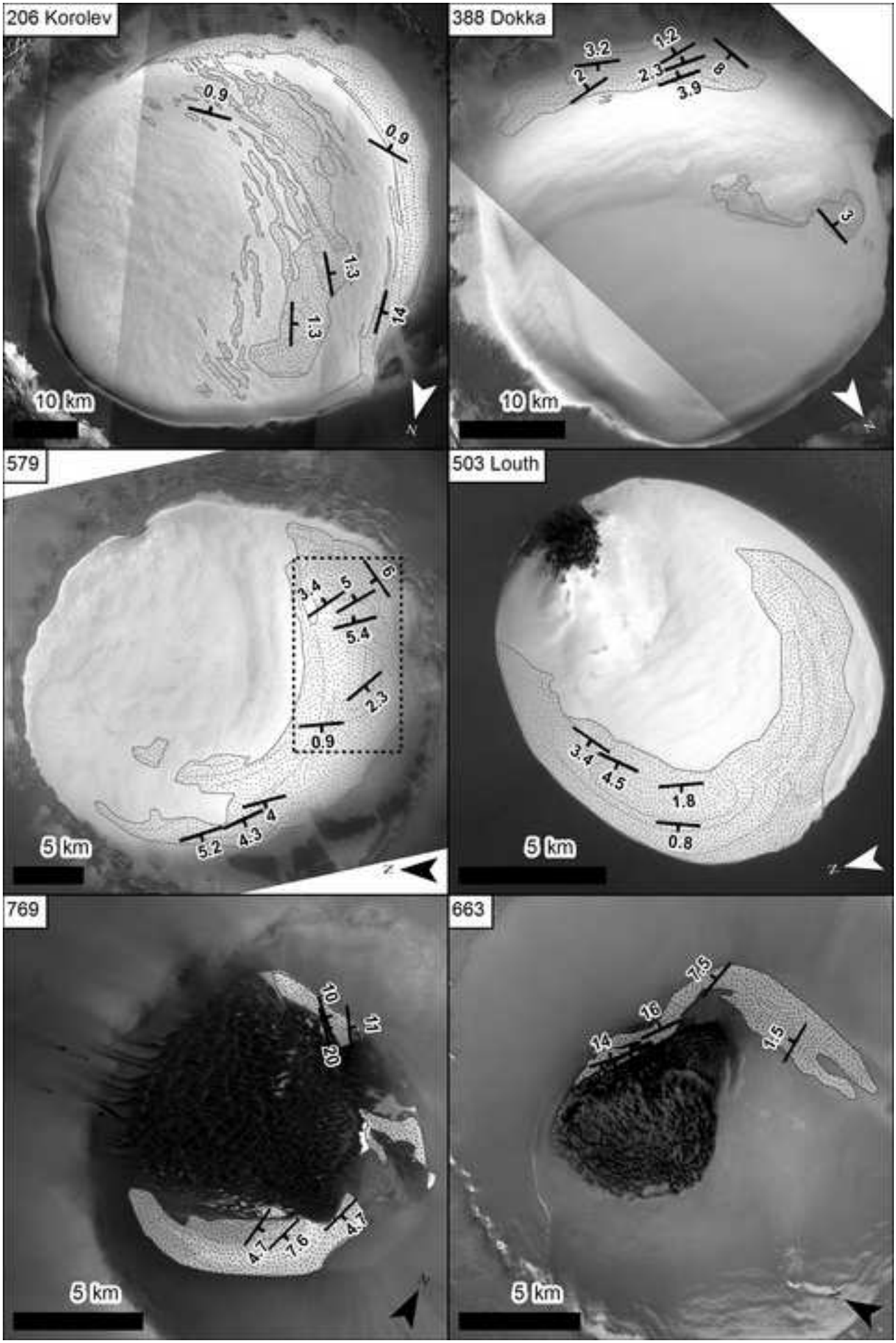

Figure 7

Click here to download high resolution image

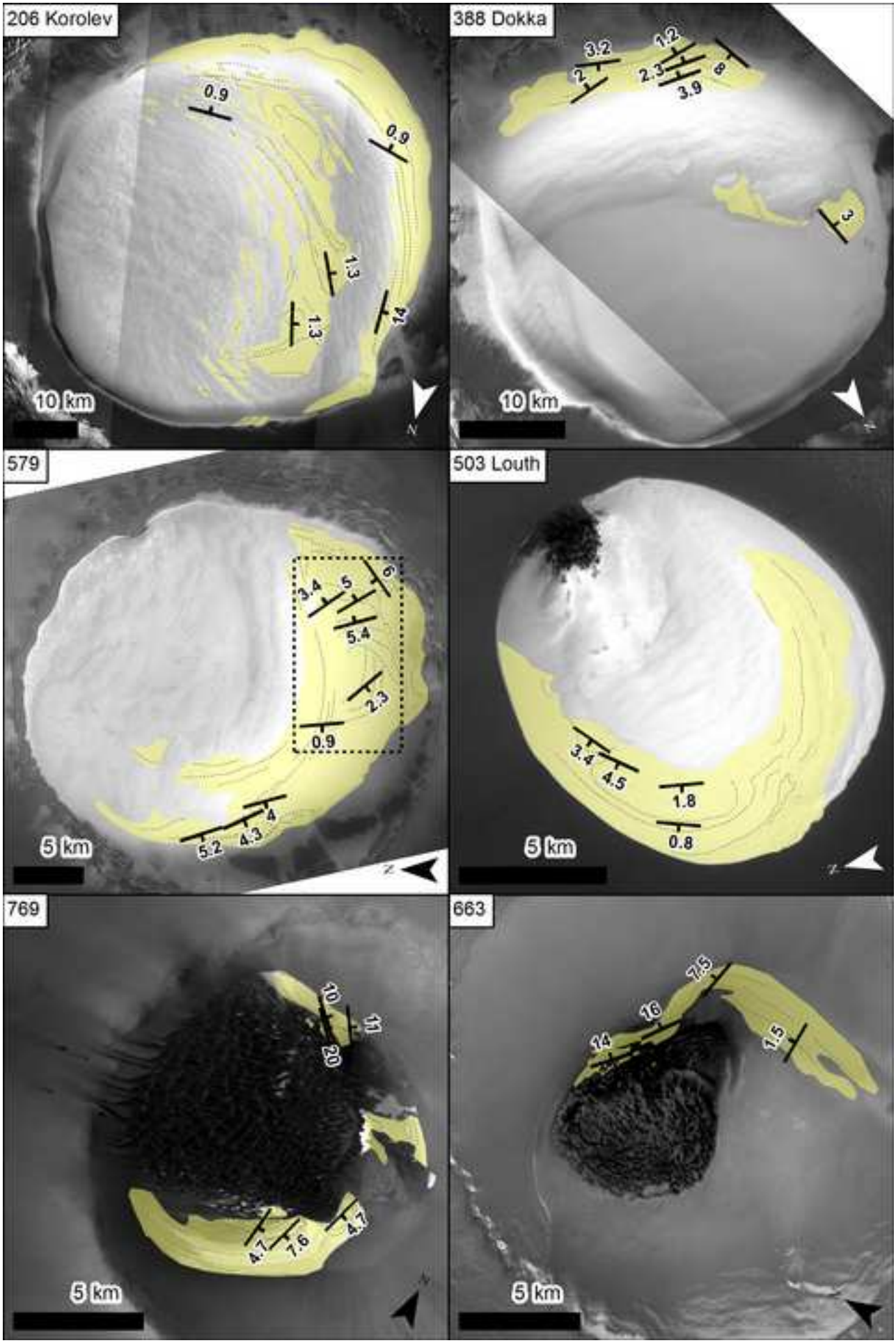

Figure 8 (black and white)

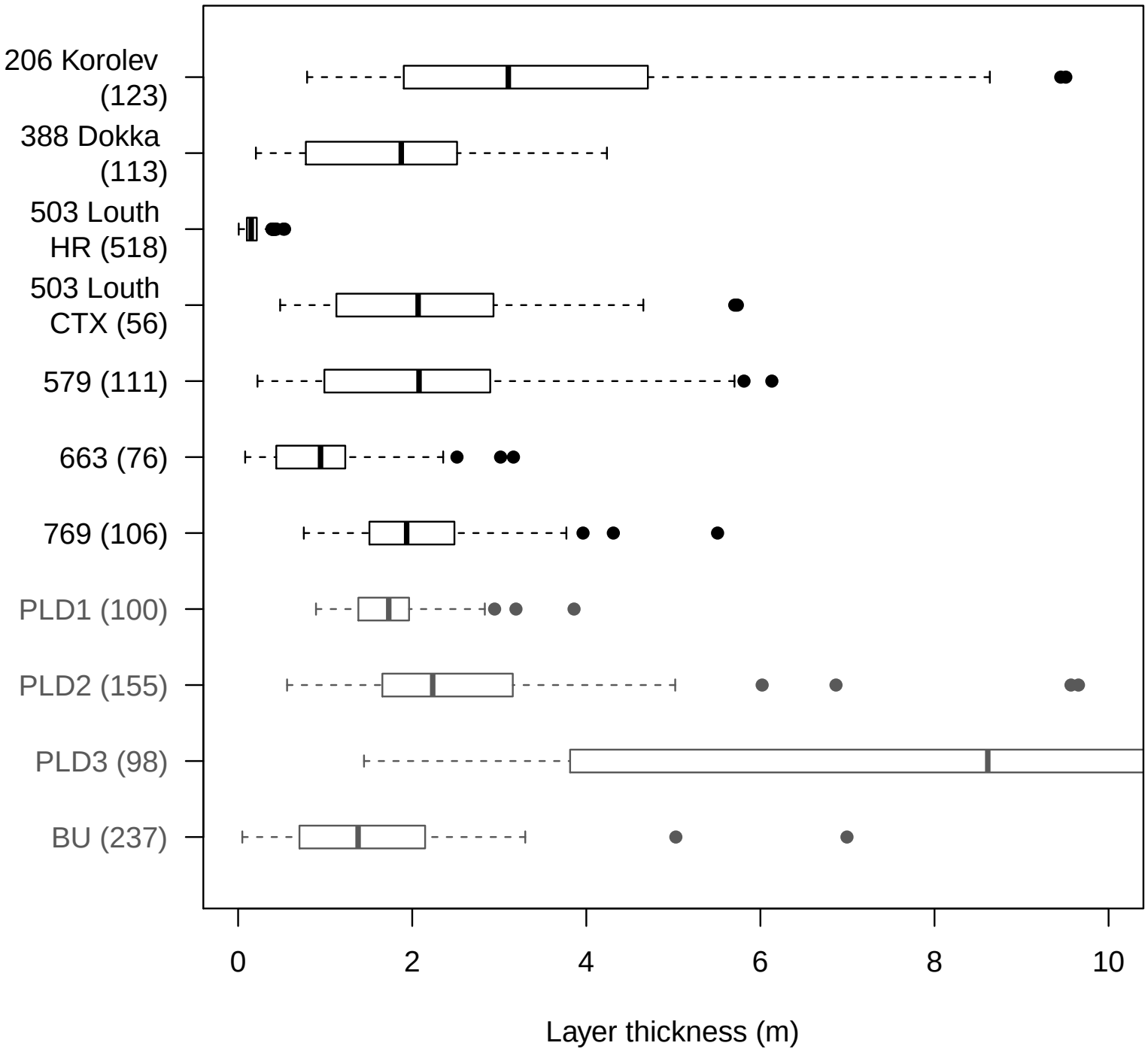

Figure 9 (black and white)

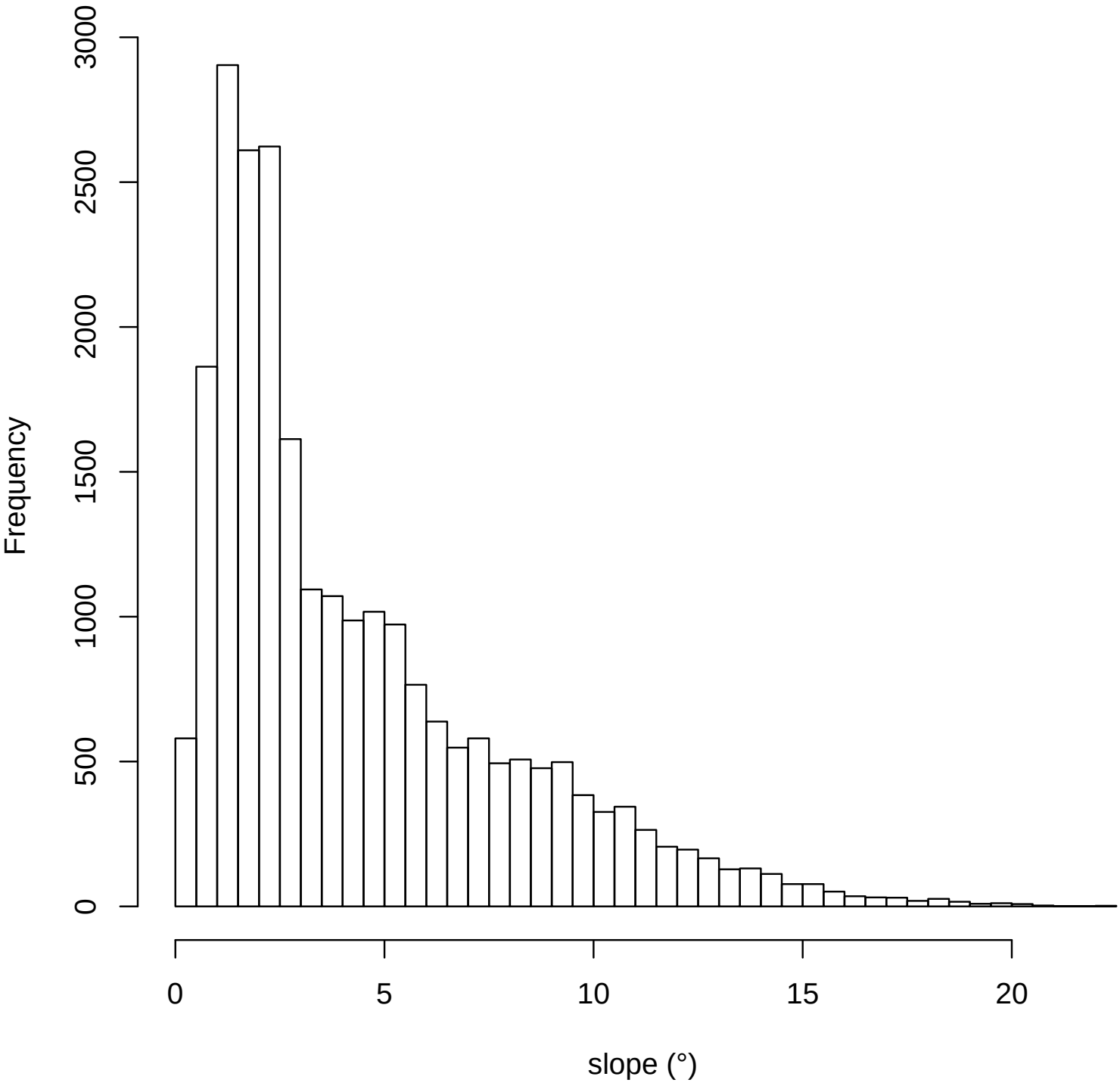

Figure 10 (black and white)
Click here to download high resolution image

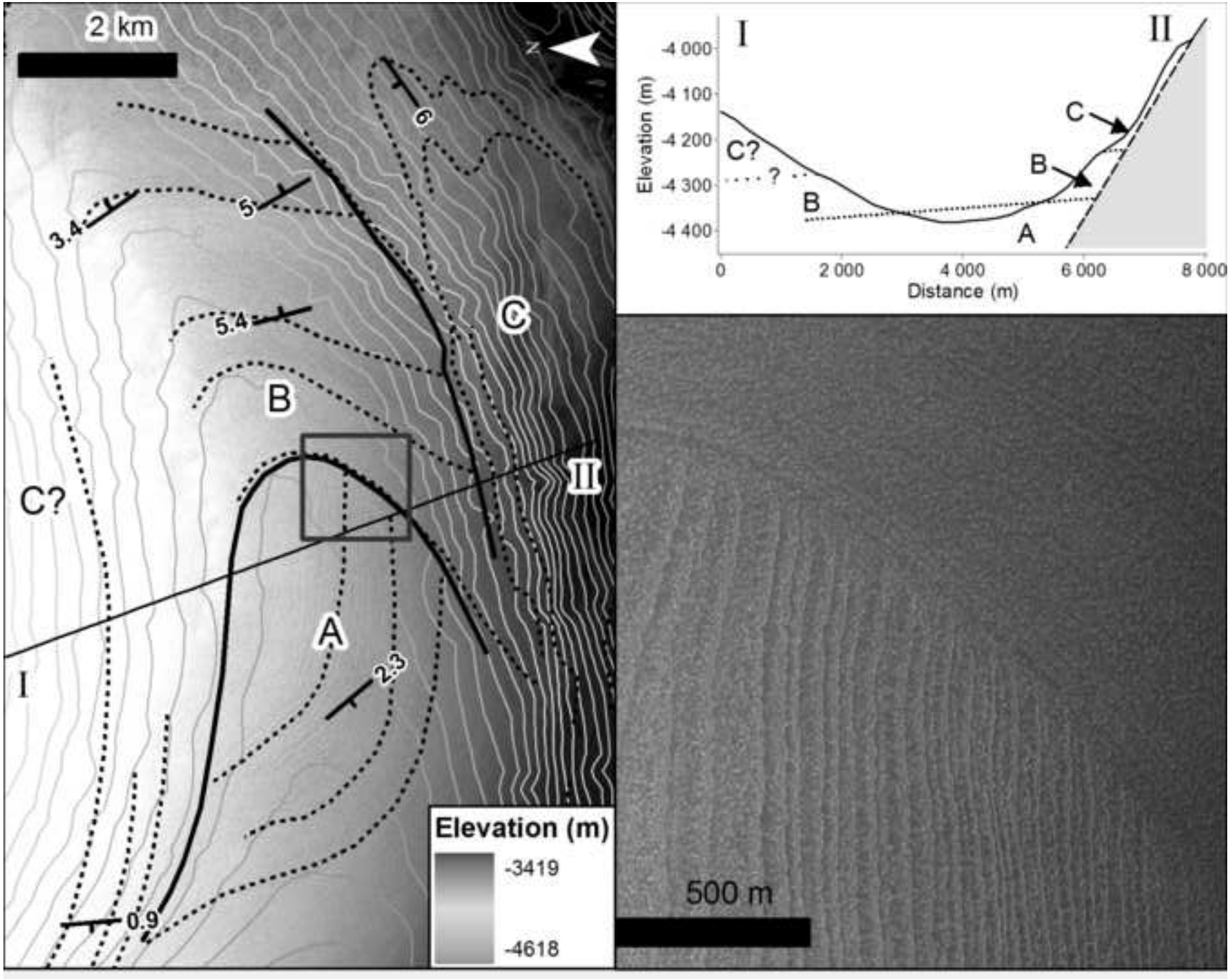

Figure 10

Click here to download high resolution image

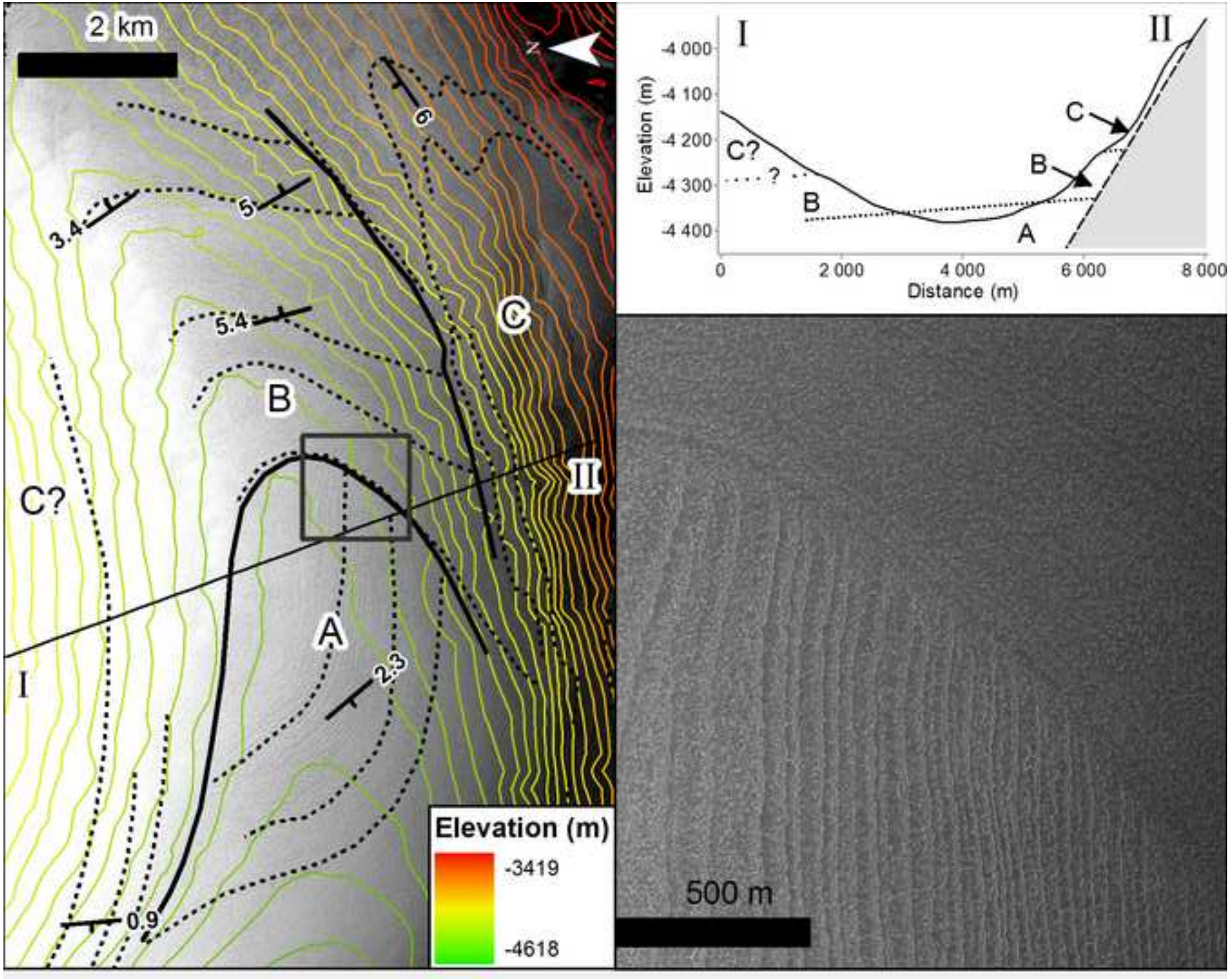

Figure 11 (black and white)
Click here to download high resolution image

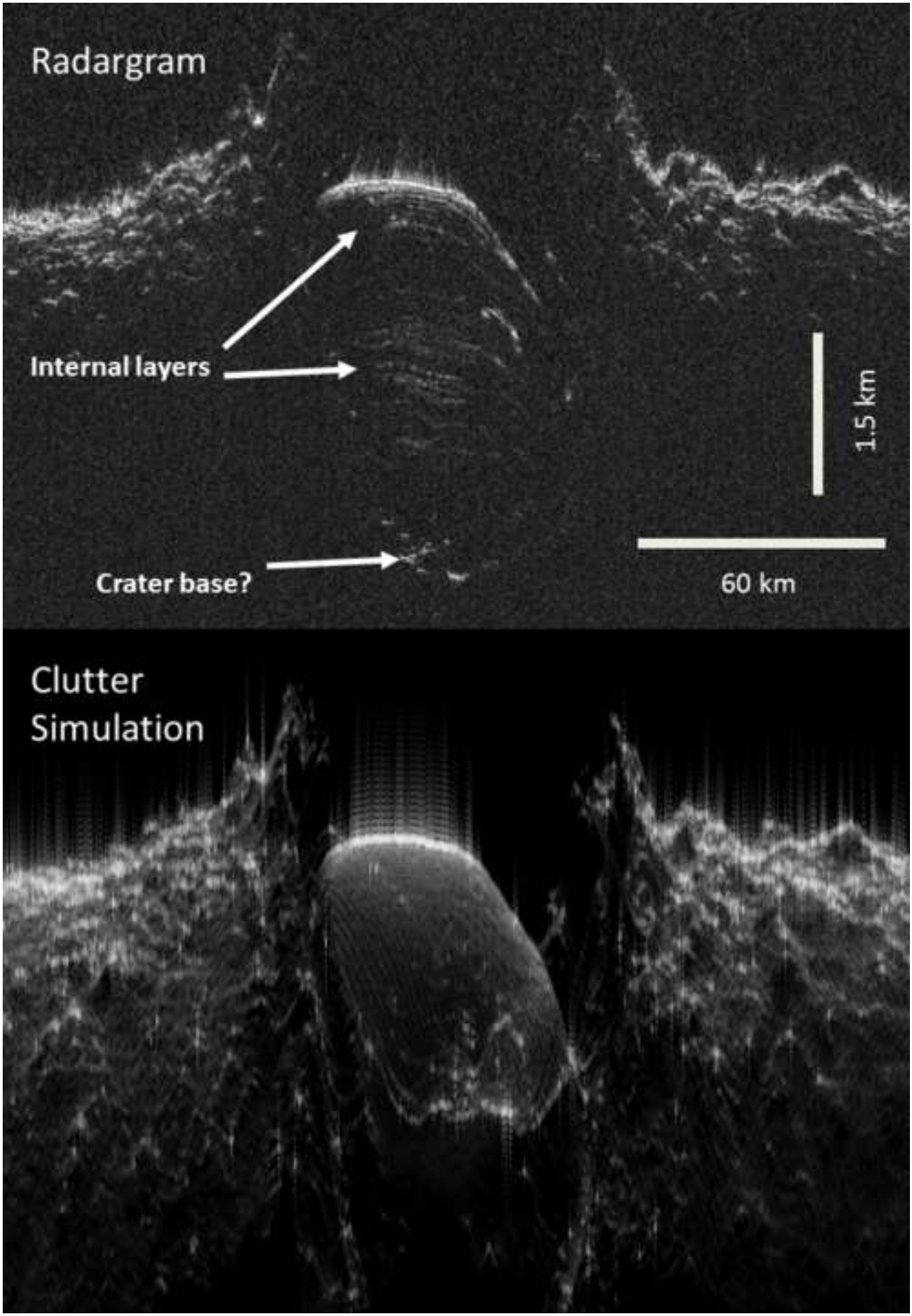

Figure 12 (black and white)
Click here to download high resolution image

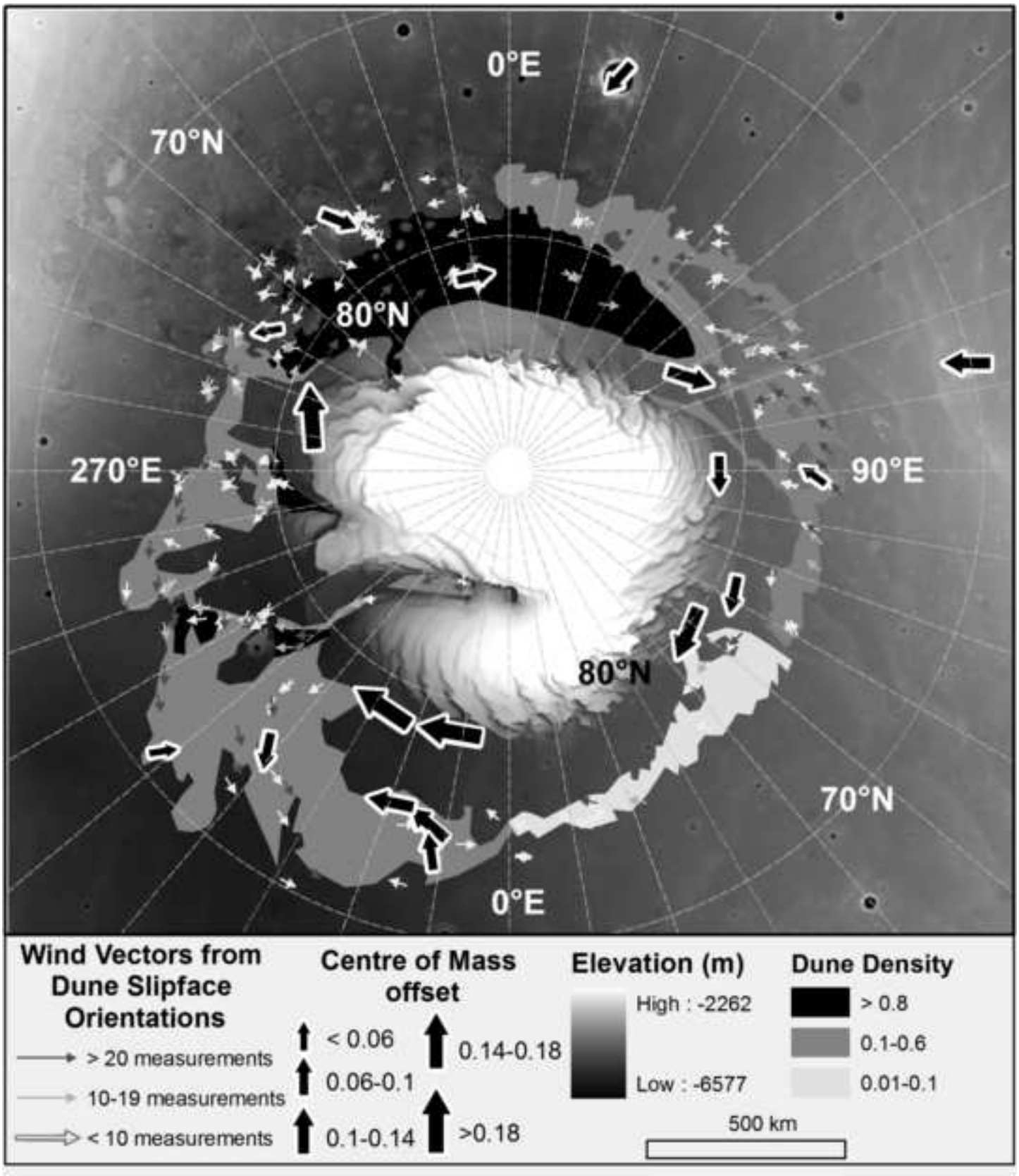

Figure 12

Click here to download high resolution image

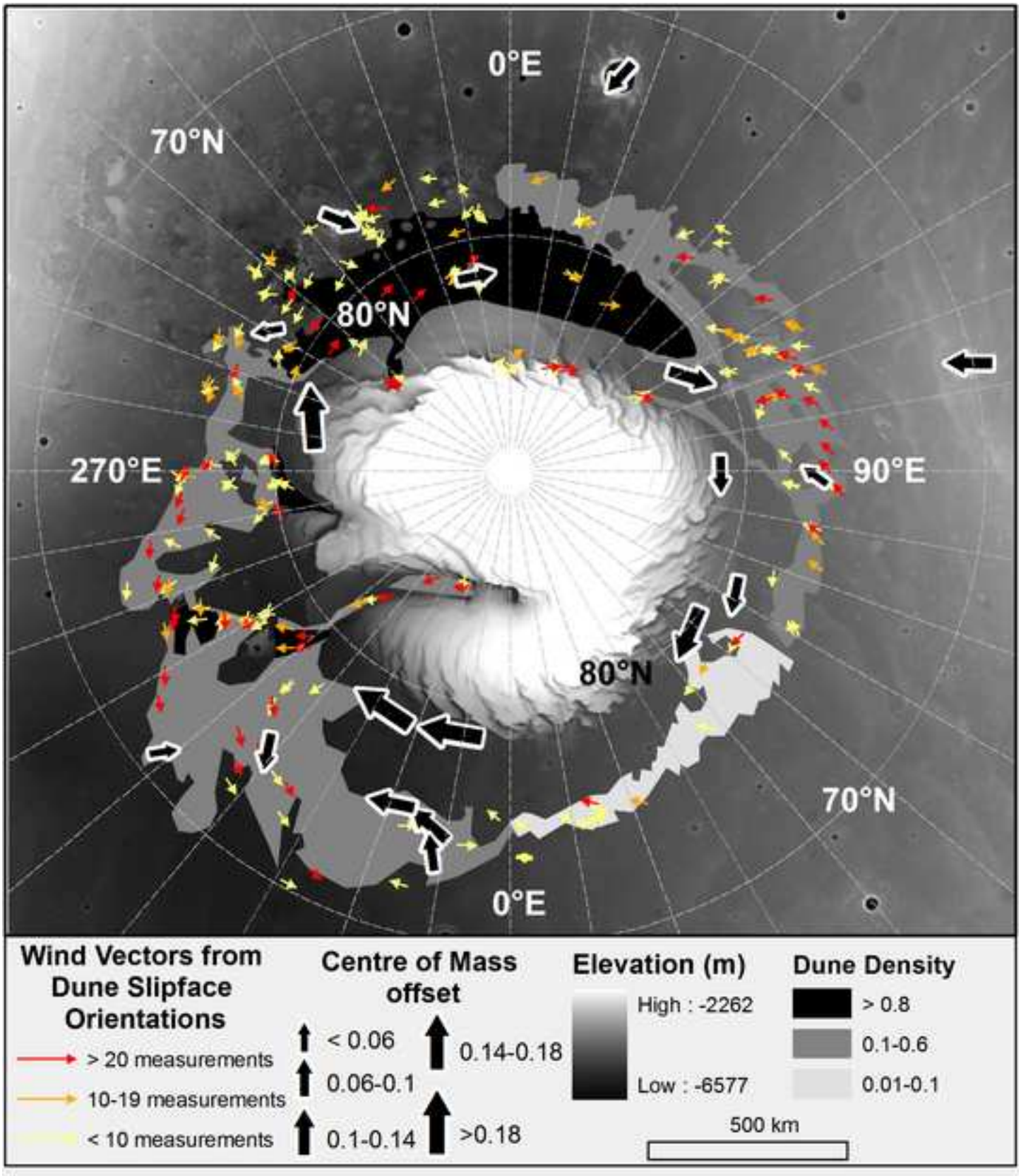

Figure13 (black and white)

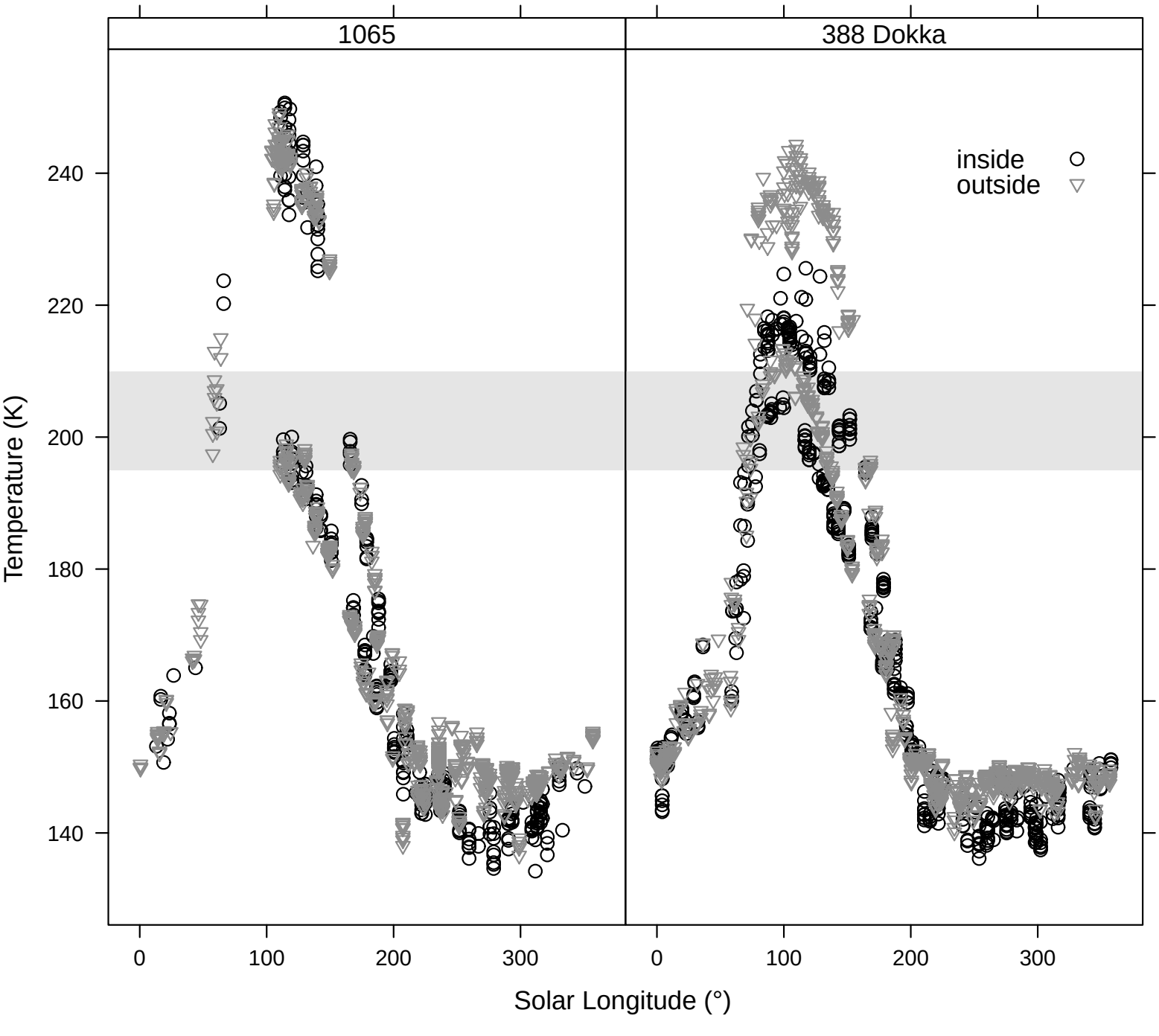

Figure13

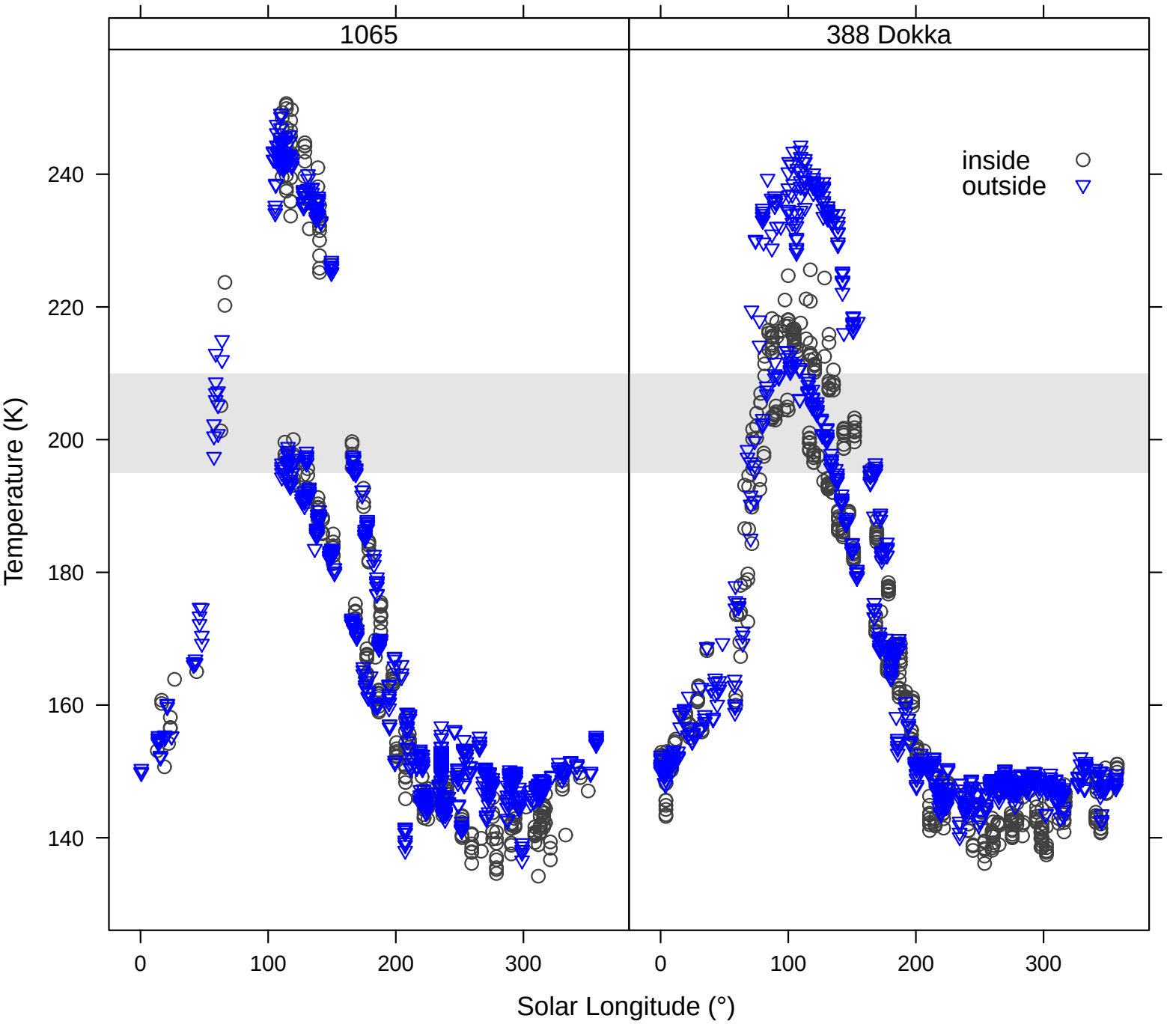
1065
388 Dokka
inside
outside
Temperature (K)
240
220
200
180
160
140
0
100
200
300
Solar Longitude (°)

Figure 14 (black and white)
Click here to download high resolution image

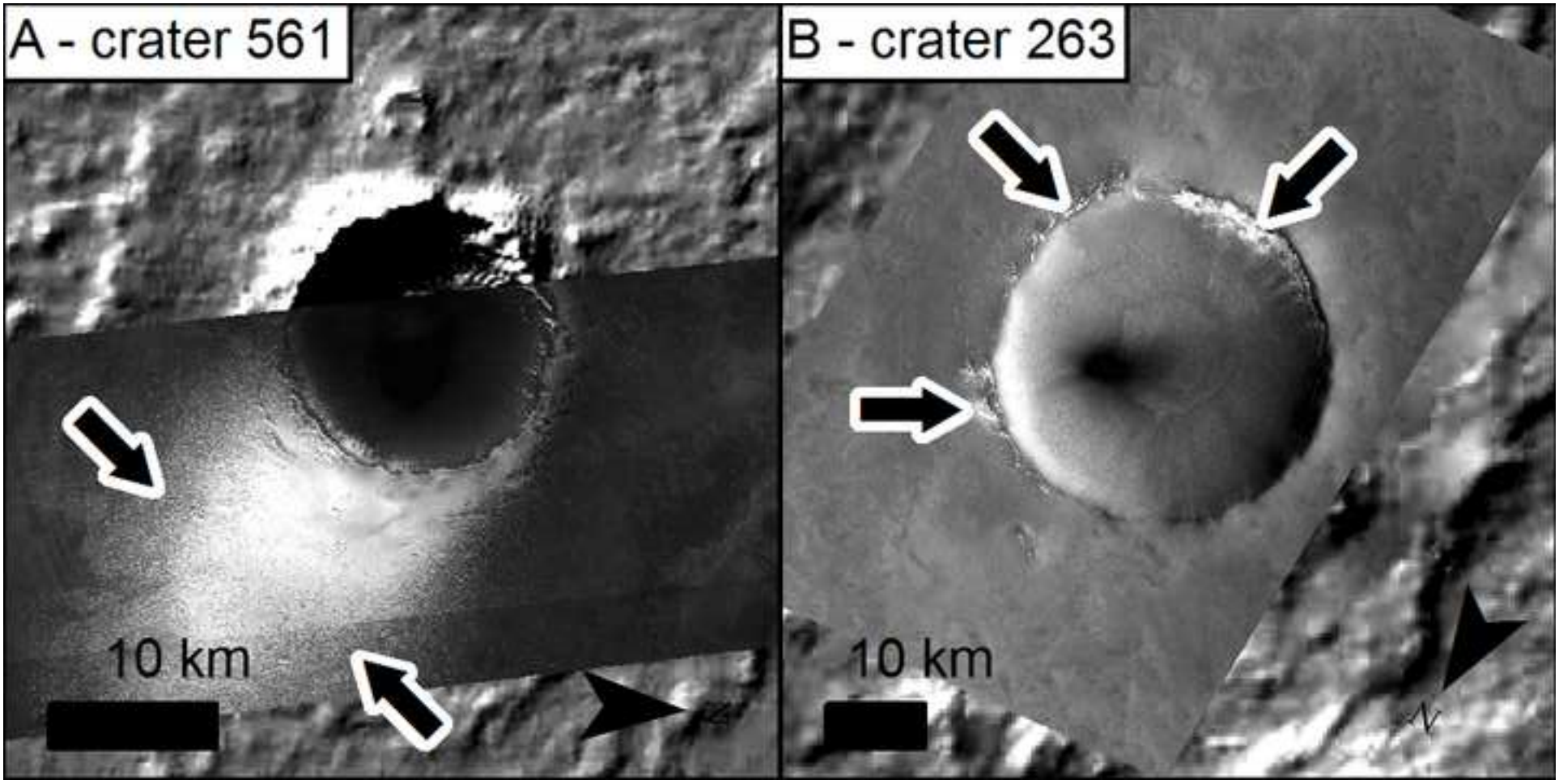

Figure 15 (black and white)
Click here to download high resolution image

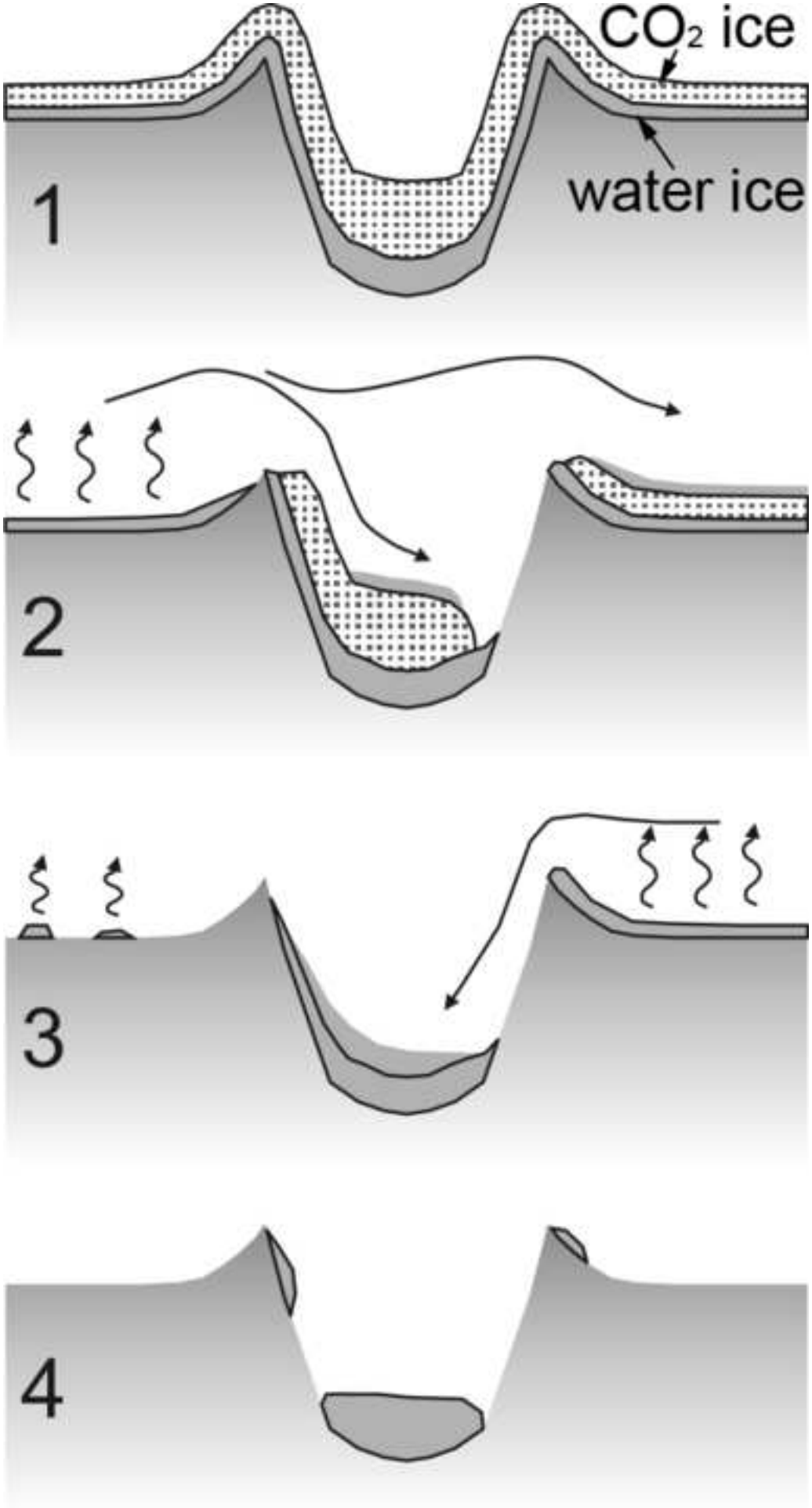

Figure 15

Click here to download high resolution image

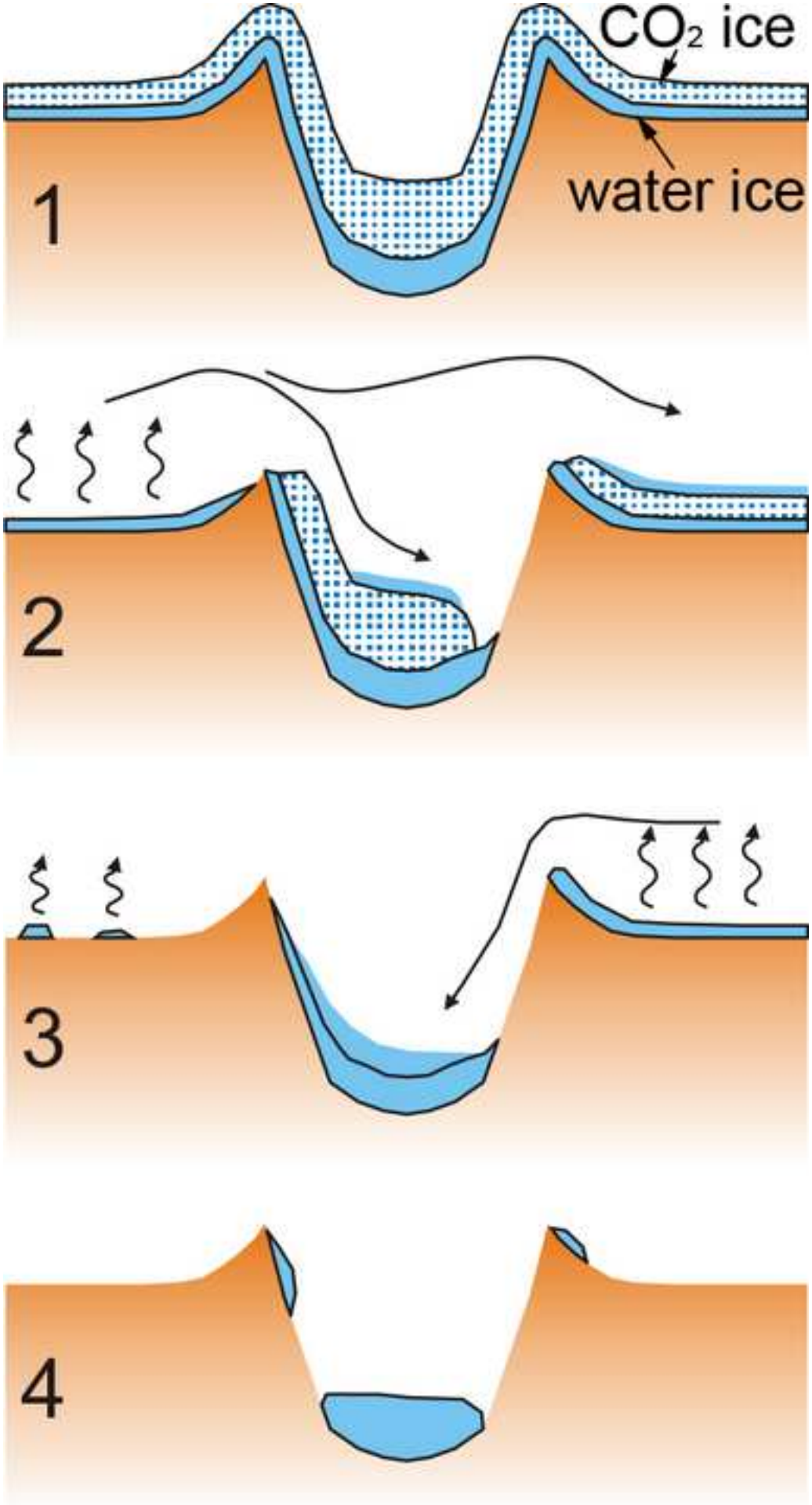

Figure 16 (black and white)
Click here to download high resolution image

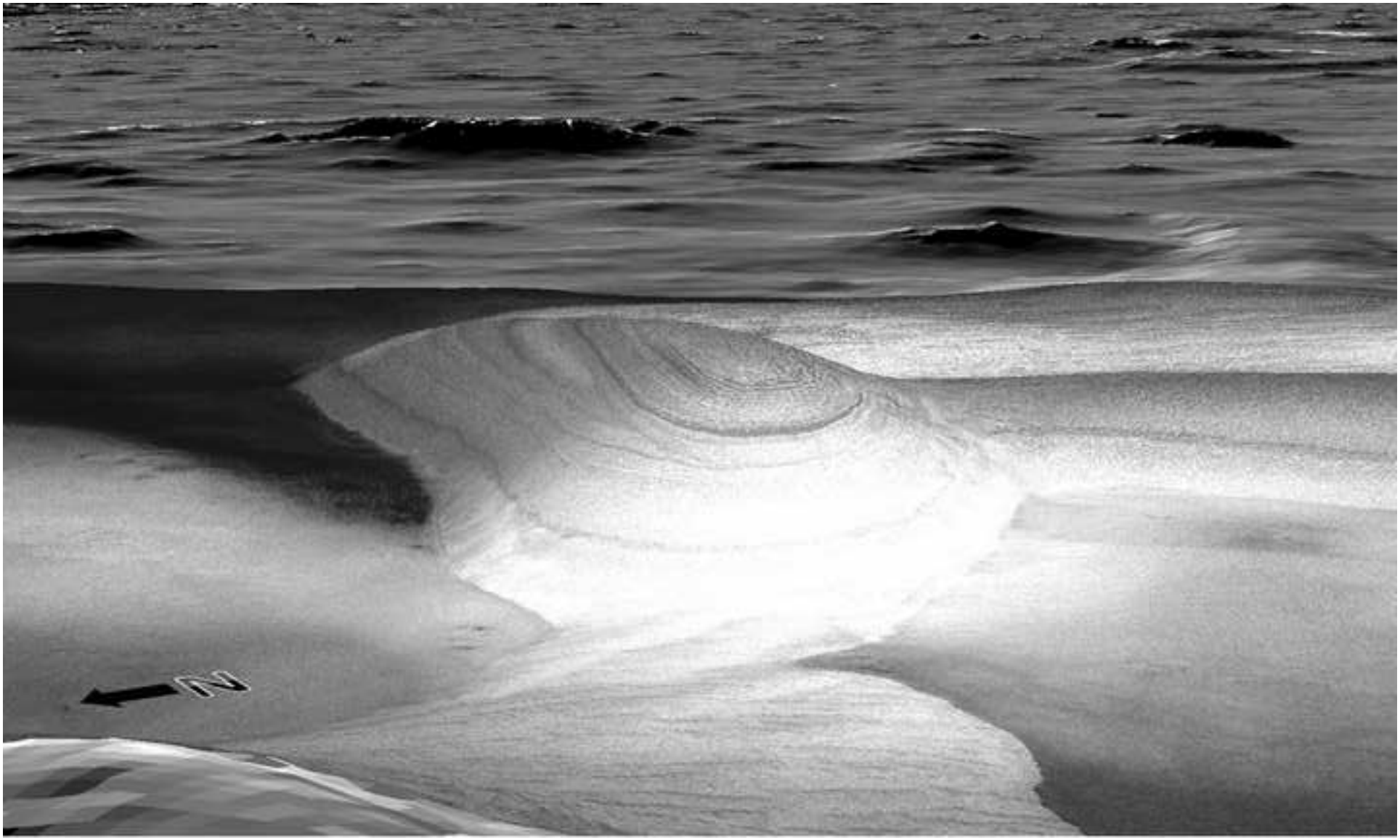

Sup. Mat. Fig. S1

Click here to download Supplementary Material for on-line publication only: AllCrossSections.tif